

Origin of low Mg# hawaiites carrying peridotite xenoliths from the Cima volcanic field, California, USA: Evidence of rapid magma mixing during ascent along intersecting fractures

Sarah K. Brehm[†], and Rebecca A. Lange

Department of Earth and Environmental Sciences, University of Michigan, 2534 North University Building, 1100 North University Avenue, Ann Arbor, Michigan 48109-1005, USA

ABSTRACT

The Cima volcanic field, in the southern Basin and Range province (California, USA), includes >70 eruptive units over the last 8 m.v. The voungest (≤1 Ma) are low Mg# (≥56) hawaiites derived from an asthenospheric mantle source. The Cima hawaiites, and adjacent Dish Hill basanites, are known for carrying large mantle xenoliths, which precludes stalling in a crustal reservoir. This raises the question of how low Mg# hawaiites, which cannot be in equilibrium with peridotite mantle, formed and differentiated while carrying dense, mantle xenoliths. Several hypotheses are evaluated and the only one shown to be viable is mixing between high-MgO basanite (with entrained mantle xenoliths and sparse olivine phenocrysts) and low-MgO mugearite liquids, which formed by partial melting of mafic lower crust under relatively dry and reducing conditions. Multiple lines of evidence, including the presence of mantle xenoliths in hawaiites, diffusion-limited growth textures in olivine and clinopyroxene, and notably thin Fe-rich rims on high-MgO olivine crystals (inherited), indicate magma mixing must have occurred rapidly (days or less) during ascent to the surface along intersecting fractures, and not in a stalled crustal reservoir. Abundant evidence points to clinopyroxene growth immediately after mixing, and application of clinopyroxene-melt barometry constrains the depth of mixing to the lower and middle crust (0.8-0.4 GPa). Results from olivinemelt thermometry/hygrometry (~1196 °C and ~1.4 wt% H₂O) applied to a basanite from Dish Hill carrying 5-20 cm mantle xe-

Sarah K. Brehm https://orcid.org/0000-0001-7880-1869

noliths leads to calculated ascent velocities \geq 0.3–4.9 km/h, enabling ascent through the 36 km thick crust in \leq 7–119 h.

INTRODUCTION

The Cima volcanic field and the nearby Dish Hill volcanic cone, located in the Mojave Desert in southeastern California, are among many localities in the western United States that are known for lavas that carry mantle peridotite xenoliths (e.g., Wilshire et al., 1988, 1991; Farmer et al., 1995; Wilshire and McGuire, 1996; Mukasa and Wilshire, 1997; Luffi et al., 2009; Baziotis et al., 2017, 2019). This requires that these magmas ascended rapidly to the surface without stalling in crustal magma chambers, otherwise the mantle xenoliths would settle out. For peridotite-bearing lavas that are MgO-rich, and thus close representatives of partial melts of the mantle, there is an opportunity to apply olivine-melt thermometry and hygrometry at the onset of olivine phenocryst growth during ascent. This approach was demonstrated to be effective for basalts carrying mantle xenoliths from the Big Pine volcanic field in California (Brehm and Lange, 2020). In Brehm and Lange (2020), the hygrometry results give water contents that match those analyzed directly in olivine-hosted melt inclusions in Big Pine basalts (1.5-3.0 wt% Gazel et al., 2012).

One of the primary goals of this study is to apply a similar approach to lavas from the Cima volcanic field (and Dish Hill) to obtain temperatures and water contents at the liquidus. Because direct analyses of water contents in olivine-hosted melt inclusions from Cima lavas are available (Plank and Forsyth, 2016), the accuracy of the hygrometry results can be independently evaluated. The resulting temperatures and melt water contents can then be compared between mafic melts derived from two distinctly different mantle sources. Whereas the Big Pine

basalts have a geochemical signature that indicates a subduction-modified lithospheric mantle source (e.g., Gazel et al., 2012; Putirka et al., 2012), the Cima and Dish Hill lavas have trace-element contents and isotopic ratios that indicate an origin in the asthenosphere (e.g., Farmer et al., 1995; Shervais et al., 1973; Wilshire and Trask, 1971). An additional objective is to test whether clinopyroxene-liquid barometry can be applied at the onset of clinopyroxene growth.

Another main goal of this study is to understand why several of the peridotite-bearing Cima lavas are so low in MgO content (≥5 wt%), with Mg# values (\geq 56) too low to be in equilibrium with peridotite mantle. The challenge is to identify what differentiation process(es) enable such low-MgO melts to carry large chunks (~5 cm diameter) of dense mantle peridotite to the surface. Again, the latter observation requires rapid ascent through the crust and precludes storage in a crustal magma chamber. In this study, tests of several competing hypotheses to explain the low-MgO content of the peridotite-bearing lavas are made, including the possibility of rapid magma mixing during ascent along intersecting fractures.

TECTONIC SETTING, GEOCHEMICAL SIGNATURE, AND PREVIOUS WORK

The Cima volcanic field (~150 km²), located in the Mojave Desert in southeastern California (Fig. 1), is a part of the Basin and Range Province that has undergone lithospheric extension for the past 12 m.y., continuing to the present (e.g., Davis et al., 1993). It contains >70 lava cones and associated flows consisting of alkali olivine basalts, hawaiites, and mugearites (e.g., Wise, 1969; Wilshire et al., 1991; Farmer et al., 1995). Two pulses of volcanic activity occurred between 7.6 and 3.0 Ma and 1.0 Ma to present (Dohrenwend et al., 1984; Turrin et al., 1985). Mantle xenoliths are found in lavas from both

GSA Bulletin;

 $https://doi.org/10.1130/B36390.1;\ 18\ figures;\ 4\ tables;\ 1\ supplemental\ file.$

 $^{^\}dagger$ sbrehm@stlawu.edu.

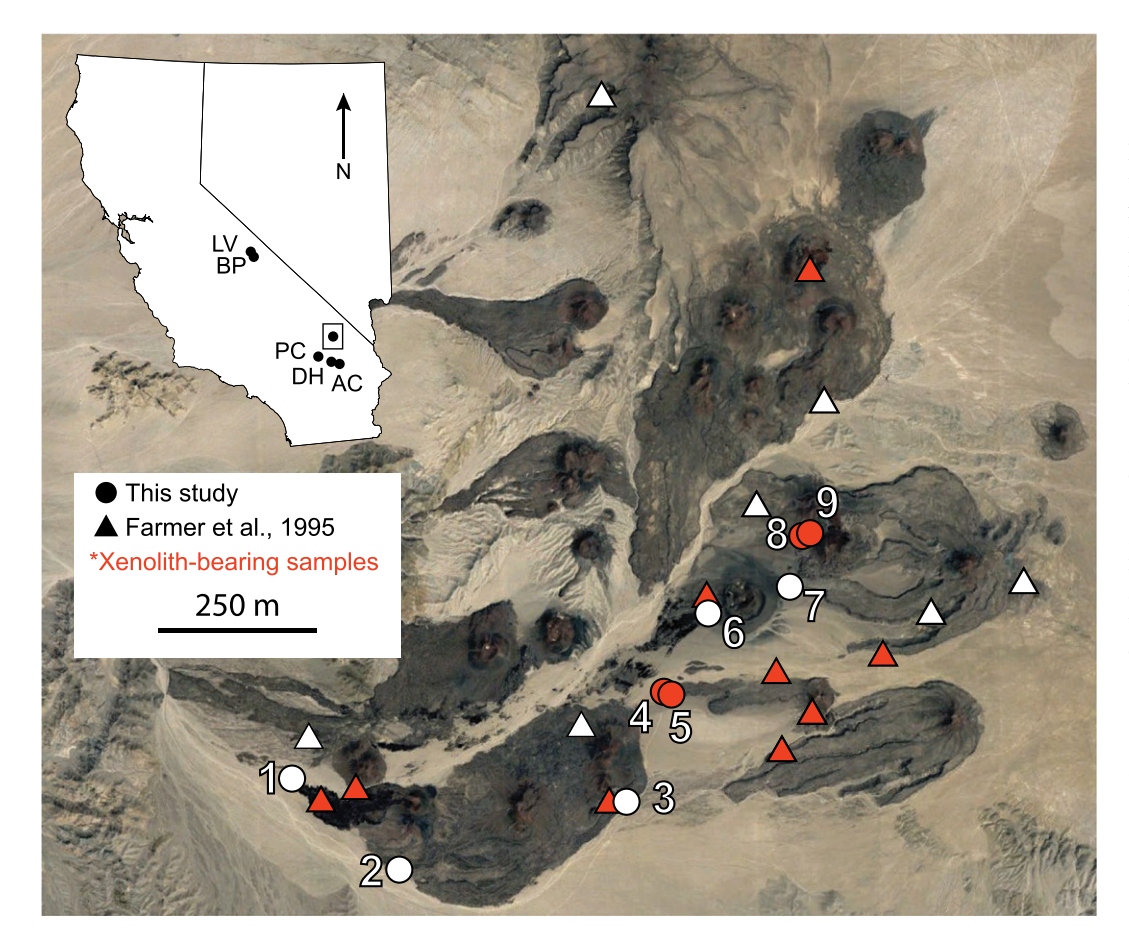


Figure 1. Google Earth map of the Cima volcanic field in California, USA depicting all sample locations from this study in solid circles. Samples from Farmer et al. (1995) are shown by solid triangles. Samples that contain mantle xenoliths from this study and Farmer et al. (1995) are highlighted in red. K-Ar dates by Dohrenwend et al. (1984) and Turrin et al. (1985) identify two distinct age groups within the Cima volcanic field including (1) ≤1 Ma and (2) 3-7 Ma. All samples in this study are from the youngest (≤1 Ma) age group. The inset map shows the locations of adjacent basaltic flows at Dish Hill (DH), Amboy Crater (AC), Pisgah Crater (PC), Big Pine (BP), and Long Valley (LV).

time periods (e.g., Wilshire et al., 1991; Mukasa and Wilshire, 1997; Luffi et al., 2009; Baziotis et al., 2017, 2019). Farmer et al. (1995) divided the Cima suite into three groups based on volcanic age, isotopic signature, and chemical composition. Group 1a lavas (≤ 1 Ma) have initial Sr and Nd isotopic values consistent with an asthenospheric mantle source (e.g., Peterman et al., 1970; Farmer et al., 1995) (Fig. 2). They contain 5.4–8.2 wt% MgO and are classified as hawaiites on a total alkali versus SiO₂ (TAS) diagram (Fig. 3). Group 1b lavas (3–5 Ma) are not

mantle-derived (3.4–5.5 wt% MgO; classified as mugearites in Fig. 3). Group 2 and Group 3 lavas (5.5–7.6 Ma) range from \sim 6 to 9 wt% MgO; they have progressively lower \mathcal{E}_{Nd} values with age relative to the Group 1 lavas (Farmer et al., 1995) (Fig. 2). Isotopic signatures of the Cima ultramafic (mantle) xenoliths are consistent with enriched lithospheric mantle, whereas mafic (gabbroic) xenoliths largely overlap the Group 1a lavas (Fig. 3), consistent with their origin as partial melts of the asthenosphere (Mukasa and Wilshire, 1997; Farmer et al., 1995).

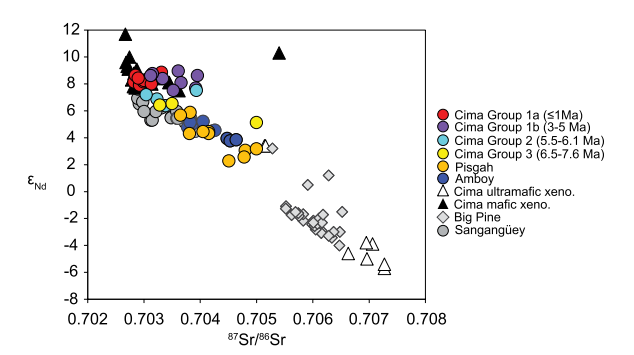


Figure 2. A plot of initial ϵ_{Nd} versus $^{87}Sr/^{86}Sr$ isotopic signatures for several samples relevant to this study (Cima volcanic field, California, USA). Data for Cima groups 1a, 1b, 2, and 3 (erupted lavas) are from Farmer et al. (1995), whereas those for Cima ultramafic and mafic xenoliths (xeno.) are from Mukasa and Wilshire (1997). Isotopic data for other

alkaline volcanic suites include Amboy and Pisgah craters (Glazner et al., 1991), the Big Pine volcanic field (Blondes et al., 2008), and the Sangangüey (Mexico) alkaline suite (Verma and Nelson, 1989; Gómez-Tuena et al., 2014; and Díaz-Bravo et al., 2014).

Plio-Quaternary alkaline volcanism is also present in neighboring regions, including Dish Hill (DH), Amboy Crater (AC), and Pisgah Crater (PC). These localities are highlighted in the inset map shown in Figure 1. Dish Hill lavas are the oldest (ca. 2.1 ± 0.2 Ma; Wilshire and Trask, 1971) and range up to 9.8 wt% MgO, whereas those from Pisgah Crater (\leq 24.2 \pm 2.7 ka; Phillips, 2003) and Amboy Crater (\leq 96.9 \pm 5.3 ka; Phillips, 2003) are younger and contain ~5–9 wt% MgO (e.g., Smith and Carmichael, 1969; Glazner et al., 1991). Dish Hill is well known for carrying peridotite mantle xenoliths, which mostly range from 5 to 10 cm in diameter but sometimes extend to 15-20 cm (e.g., Wilshire and Trask, 1971; Shervais et al., 1973; Wilshire et al., 1980; Banfield et al., 1992; Righter and Carmichael, 1993; Wilson et al., 1996; Luffi et al., 2009; Armytage et al., 2014, 2015). Mantle xenoliths have not been found in flows from Pisgah Crater or Amboy Crater.

SAMPLE LOCATIONS AND PETROGRAPHY

All 12 samples collected for this study are from the Cima volcanic field (ten; Fig. 1) and Dish Hill (two). The locations of the Cima

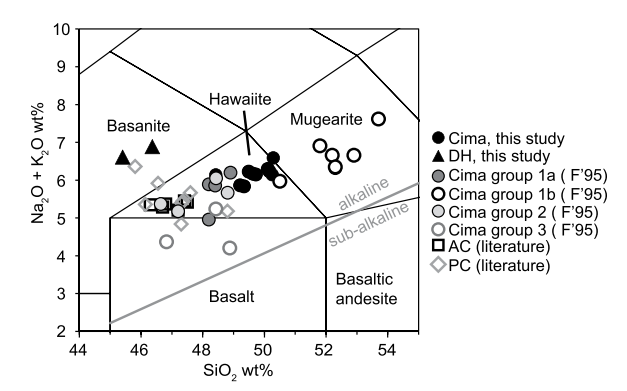


Figure 3. **Total** alkalis $(Na_2O + K_2O wt\%)$ versus SiO₂ (wt%) diagram for the Cima and Dish Hill (DH) samples (California, USA) presented in this study (closed symbols). Additional Cima volcanic samples (groups 1a, 1b, 2, and 3) are from Farmer et al. (1995). Samples from Pisgah and Amoby craters (PC and AC, respectively) are shown for comparison (Smith and Carmichael, 1969; Wise, 1969; Glazner et al., 1991; Phillips, 2003).

samples on the geological maps of Wilshire (2002a, 2002b) are shown in Figs. S1A and S1B¹. Only flows <1 Ma were targeted, and thus overlap the Group 1a suite of Farmer et al. (1995). Three separate samples (Cima-4a, -4b, and -5) were obtained from the same flow to evaluate variations in whole-rock composition and phenocryst assemblage. Mantle xenolith localities from this study and Farmer et al. (1995) are shown with red symbols. Peridotite xenoliths in flows sampled in this study are up to 9 cm in diameter (see Fig. S2, Supplemental Material). A peridotite-bearing lava from Dish Hill (Fig. 1 inset) was also sampled, and a second xenolith bearing Dish Hill sample from Ian Carmichael's collection (CC-1) is also examined in this study.

The ten Cima samples have a phenocryst assemblage of olivine + plagioclase + clinopyroxene, whereas the Dish Hill samples only contain olivine phenocrysts; clinopyroxene and plagioclase are restricted to the groundmass.

Nine of the ten Cima samples contain both titanomagnetite and ilmenite. Ilmenite is absent in Cima-1 and in the two Dish Hill samples. Chromite occurs as sparse inclusions only in olivine phenocrysts.

ANALYTICAL METHODS

Whole-Rock Major- and Trace-Elements

Ten samples from the Cima volcanic field and two from Dish Hill were crushed and powdered in a tungsten carbide shatterbox. Majorand trace-element analyses were performed by inductively coupled plasma—mass spectrometry at Activation Laboratories, Ontario, Canada. Whole-rock Ni analyses were also performed at Activation Laboratories via single element pressed pellet X-ray fluorescence.

Electron Microprobe Analyses of Mineral Phases

The compositions of olivine, clinopyroxene, Fe-Ti oxides, and plagioclase crystals in the Cima and Dish Hill samples were analyzed using a Cameca SX-100 electron microprobe at the Robert B. Mitchell Electron Microbeam Analysis Lab at the University of Michigan, Ann Arbor, Michigan, USA. Crystalline standards for all analyses are contained in the University of Michigan collection and are presented in Table S1 (see footnote 1). Details for the plagioclase analyses are presented in the supplemental file, whereas those for olivine, clinopyroxene, and the Fe-Ti oxides are presented below.

Analyses of olivine phenocrysts in the ten Cima and two Dish Hill samples, as well as olivine crystals in a mantle xenolith entrained in Cima-4a, were obtained using a focused beam with an accelerating voltage of 20 kV and a 40 nA current. Eight elements (Mg, Al, Si, Ca, Cr, Mn, Fe, Ni) were analyzed with individual

peak and background counting times of 30 and 20 s, respectively, for Mg, Fe, Si, and Ni, and 20 s each for Al, Ca, Cr, and Mn. The 1σ error based on counting statistics are $\pm 0.29~\text{SiO}_2,~\pm 0.21~\text{MgO},~\pm 0.31~\text{FeO}^T,~\pm 0.02~\text{NiO},~\pm 0.02~\text{Cr}_2\text{O}_3,~\pm 0.02~\text{Al}_2\text{O}_3,~\pm 0.02~\text{CaO},~\text{and}~\pm 0.05~\text{MnO}$ wt%. Analytical transects were collected for a total of 43–100 olivine phenocrysts per sample with individual spot analyses every 25–35 $\mu\text{m},~\text{yielding}$ between 198 and 745 analyses per sample. Analyses were filtered to exclude those with analytical totals outside 99–101 wt%.

Analyses of clinopyroxene phenocrysts were obtained on five representative samples (Cima-1, -2, -3, -5, and -8) using a 20 kV accelerating voltage and a focused beam with a 20 nA current. Ten elements (Na, Mg, Al, Si, Ca, Ti, Cr, Mn, Fe, Ni) were analyzed with peak and background counting times of 20 s each. The 1σ error based on counting statistics are ± 0.06 Na₂O, ± 0.16 MgO, ± 0.13 Al₂O₃, ± 0.65 SiO₂, ± 0.23 CaO, ± 0.08 TiO₂, ± 0.03 Cr₂O₃, ± 0.03 MnO, $\pm 0.17 \text{ FeO}^{\text{T}}$, and $\pm 0.03 \text{ NiO wt}\%$. Analytical transects across 42-83 clinopyroxene phenocrysts per sample were collected with individual spot analyses every 25-35 μm, yielding 197-335 analyses per sample. Clinopyroxene analyses were filtered to exclude analytical totals outside 98.5-100.5 wt%.

Titanomagnetite and ilmenite grains large enough for analysis were found in eight and six Cima samples, respectively. Nine elements (Si, Ti, Al, Fe, V, Cr, Mn, Mg, Ca) were analyzed with a focused beam, a 15 kV accelerating voltage, and a 10 nA current. Peak and background counting times are 20 s each. Single spot analyses of ilmenite and titanomagnetite were collected and FeO and Fe2O3 are calculated based on cation stoichiometry. Analyses were filtered to exclude those with >0.25 wt% SiO₂ or CaO and analytical totals outside 98-101 wt%, yielding between 3 and 44 analyses per sample. For ilmenite the 1σ error from counting statistics are ± 0.10 MgO, ± 0.13 Al₂O₃, ± 0.26 SiO₂, ± 0.11 CaO, $\pm 0.08 \text{ V}_2\text{O}_5$, $\pm 0.06 \text{ Cr}_2\text{O}_3$, $\pm 0.09 \text{ MnO}$, ± 0.59 FeO^T, and ± 0.64 TiO₂. For titanomagnetite the 1σ error from counting statistics are ± 0.13 MgO, ± 0.14 Al₂O₃, ± 0.12 SiO₂, ± 0.08 CaO, ±0.09 V₂O₅, ±0.07 Cr₂O₃, ±0.09 MnO, $\pm 0.81 \text{ FeO}^{\text{T}}$, and $\pm 0.53 \text{ TiO}_2$.

X-ray intensity maps of P and Fe for the most forsteritic olivine analyzed in three samples (Cima-8, -3, CC-1) were collected using a 15 kV accelerating voltage and a 200 nA beam current. Wavelength dispersive spectroscopy maps were collected with P on four spectrometers and Fe on the fifth with dwell times of 200–300 µsec/pixel. Back-scattered electron images for all analyzed olivine, clinopyroxene, and plagioclase crystals were collected.

¹Supplemental Material. Table S1: Standards employed for electron microprobe analyses of olivine, clinopyroxene, plagioclase, and Fe-Ti oxides. Table S22: Analyzed trace-element concentrations for all Cima samples. Table S3: Olivine phenocryst analyses for all Cima and Dish Hill samples. Table S4: (A) Clinopyroxene analyses for five Cima hawaiites. (B) Composition of the most Mg-rich clinopyroxene phenocryst. Table S5: (A) Microprobe analyses of ilmenite and titanomagnetite from six Cima hawaiites. (B) Fe-Ti oxide thermometry and oxybarometry (Ghiorso and Evans, 2008) results for all possible pairs of ilmenite and titanomagnetite. (C) Composition (wt%) of onset ilmenite and titanomagnetite pair that pass the Bacon and Hirschmann (1988) test for equilibrium. Table S6: (A) Plagioclase phenocryst analyses for three Cima hawaiites. (B) Analysis of most calcic plagioclase phenocryst. Table S7: Olivine-melt thermometry applied to all Cima and Dish Hill samples. Please visit https://doi.org/10.1130/GSAB.S.19633134 to access the supplemental material, and contact editing@geosociety.org with any questions.

Cima-7 15°45.752 35°12.059 *Cima-5 35°12.071 'Cima-4a 35°12.071 *Cima-4b QTf8-2 TABLE 1.WHOLE-ROCK MAJOR-ELEMENTS (WT%) AND SELECT TRACE ELEMENTS (PPM) 35°10.182 Cima-2 35°12.890' 115°45.167' V13 QTf13-1 Cima-6 35°13.779′ 115°43.901′ Cima-9 35°11.141' 115°50.652' V3 QTf2-1 Cima-1 35°13.741 *Cima-8 V14 OTf14-1 35°10.925 V6 OTf7-3 34°36.472′ 115°57.055′ H

Notes: Major element oxide components normalized to 100% and presented with original totals and loss on ignition(LOI). Lat—latitude; Long—longitude.

*Mantle xenolith bearing. The second representation of the second secon

ANALYTICAL RESULTS

Whole-Rock Major- and Trace-Element Analyses

All whole-rock major-element oxide components are normalized and presented with original totals and loss on ignition in Table 1. In this study, the total alkali versus SiO₂ (TAS) diagram is used to classify samples (Fig. 3). The two Dish Hill samples are basanites and have relatively high MgO (7.5–9.8 wt%) and Ni (138–197 ppm) contents, whereas the Cima samples from this study (and most Group 1a samples from Farmer et al., 1995) are hawaiites and contain 5.5–7.1 wt% MgO and 61–90 ppm Ni. Note that the Group 1b samples from Farmer et al. (1995) are mugearites in the TAS diagram (Fig. 3).

Whole-rock major-element compositions for the three samples taken from the same flow (Cima-4a, -4b, and -5; Fig. 1) show little variability (within 0%–2% relative; Table 1) in the flow and good analytical reproducibility. Note that this flow has a relatively low Mg# of \sim 56 (Table 1), and yet it contains peridotite xenoliths.

Select trace element concentrations and ratios are shown in Table 1, whereas all analyzed trace element concentrations are presented in Table S2 (see footnote 1). A plot of Ba/La versus Nb/Zr (Fig. 4) confirms an asthenospheric source for the Cima and Dish Hill samples, as previously demonstrated in the literature (e.g., Farmer et al., 1995; Wilshire and Trask, 1971; Shervais et al., 1973). In contrast, the Big Pine basalts from Brehm and Lange (2020) have elevated Ba/La ratios consistent with a subduction-modified lithospheric mantle source (Gazel et al., 2012; Putirka et al., 2012). Also shown in Figure 4 are results for other basaltic suites for which the olivine-melt thermometer and hygrometer of Pu et al. (2017, 2021) have been applied and are discussed later in the section on hygrometry.

Variation diagrams of wt% SiO₂, Al₂O₃, TiO₂, FeO^T, CaO, P₂O₅, Na₂O, and K₂O versus wt% MgO for the Cima and Dish Hill basalts are presented in Figure 5. In addition to the samples from this study, Group 1a and Group 1b Cima samples from Farmer et al. (1995) are also shown, as well as high-MgO (≥8 wt%) samples from the literature including Pisgah Crater and Amboy Crater (Wise, 1969; Smith and Carmichael, 1969; Glazner et al., 1991; Phillips, 2003). A similar set of variation plots are shown for select trace element concentrations (Cr, Ni, Sc, Ba, La, Rb, Zr, Eu) versus wt% MgO in Figure 6, using the same samples and symbols as in Figure 5. A linear fit to the Cima hawaiite data (solid black symbols) only is performed for each major- and trace-element component as a function of wt% MgO in Figures 5 and 6. An

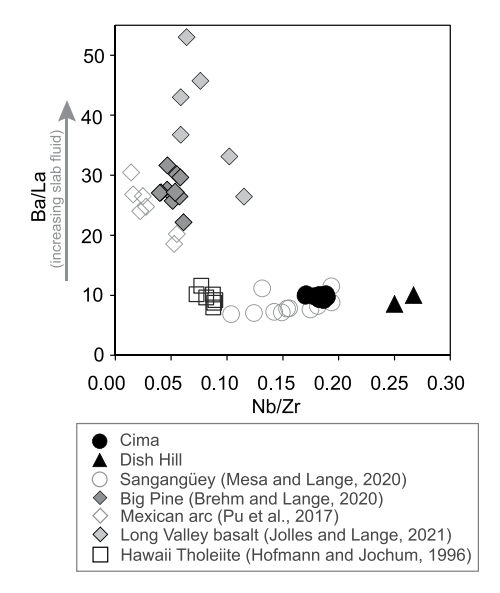


Figure 4. Ba/La versus Nb/Zr for 10 Cima basalts and two Dish Hill basalts (California, USA). Plotted for comparison are basalts from the Big Pine volcanic field (Brehm and Lange, 2020), Long Valley (Jolles and Lange, 2021), the active Mexican arc (Pu et al., 2017), Hawaiian tholeiite (Hofmann and Jochum, 1996), and the Sangangüey intraplate basalts from Mexico (Mesa and Lange, 2020). An increase in Ba/La corresponds to increased involvement of slabderived fluid (e.g., Fitton et al., 1988, 1991).

extrapolation of the linear fit to 10 wt% MgO overlaps the high-MgO basalts from Dish Hill, Pisgah, and/or Amboy in most cases, whereas an extrapolation to 4 wt% MgO broadly overlaps the low-MgO Cima mugearites (Group 1b).

Olivine Results

All individual analyses of olivine from the Cima and Dish samples are presented in Table S3 (see footnote 1). The phenocryst data are summarized for each sample in histograms of analyzed Fo content (mol%) (Fig. 7). Almost all olivine analyses are \geq Fo₇₀, and the sparse few that are as low as \sim Fo₆₆ are restricted to rim analyses. A histogram of the olivine analyses from the mantle lherzolite xenolith from Cima-4a is shown in Figure S3; all analyses cluster tightly around ~Fo₉₁, which overlaps compositions reported for olivine in Cima mantle xenoliths from Wilshire et al. (1991). The most Mg-rich olivine phenocryst analyzed in each sample is reported in Table 2 and spans a narrow range (Fo₈₆₋₈₈) for 11 of the 12 samples, despite a wide range in whole-rock MgO content (5.9-9.8 wt%). Analyzed CaO, NiO, and MnO wt% are plotted against Fo mol% (Figs. 8-10)

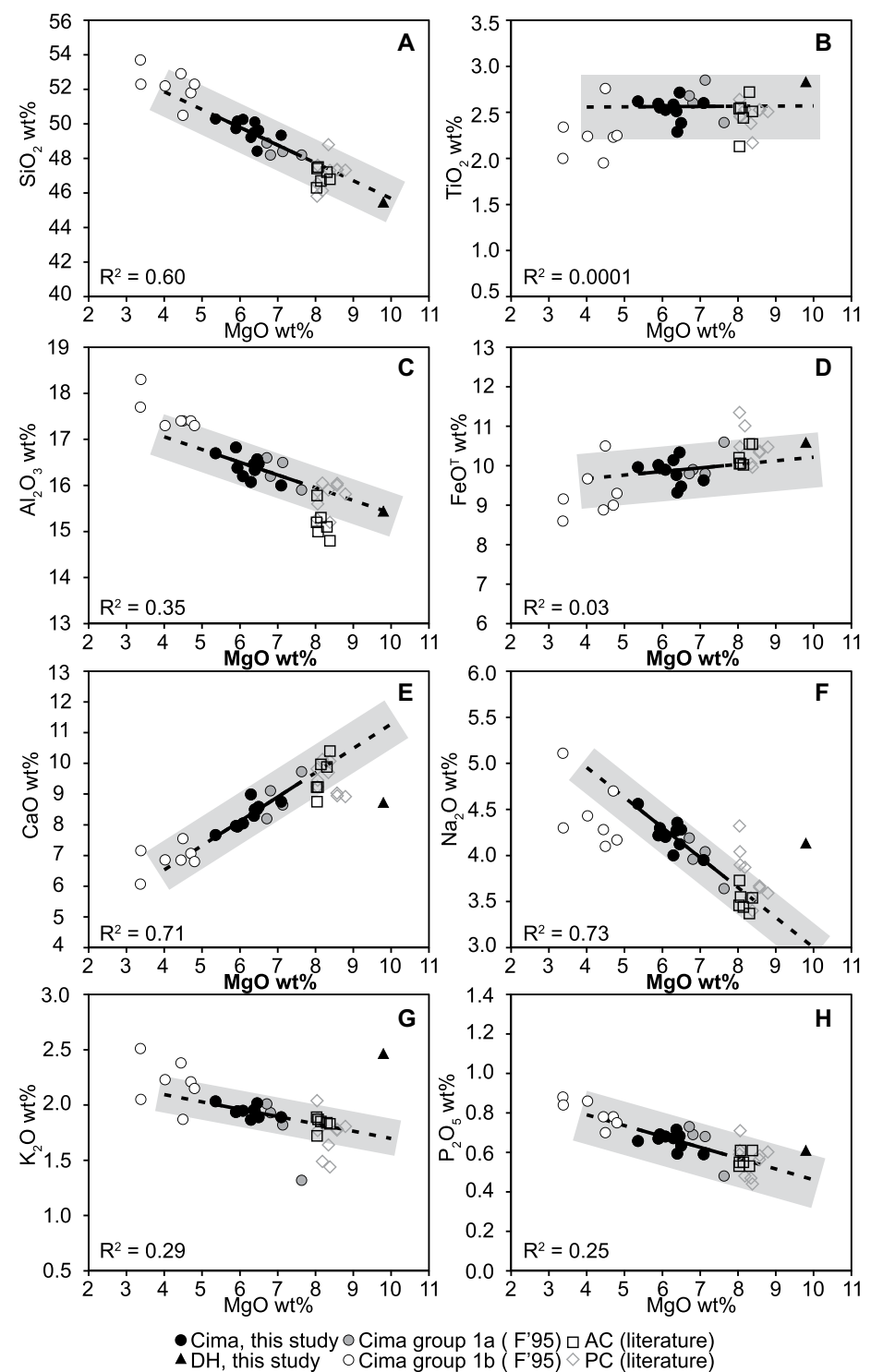


Figure 5. Whole-rock major-element variation plots versus MgO (wt%) for the Cima and Dish Hill (DH) samples (California, USA). Plotted for comparison are Group 1a and Group 1b Cima samples presented by Farmer et al. (1995), as well as whole-rock compositions from samples with >8 wt% MgO reported for Pisgah Crater (PC) (Smith and Carmichael, 1969; Wise 1969; Glazner et al., 1991; Phillips, 2003) and Amboy Crater (AC) (Smith and Carmichael, 1969; Glazner et al., 1991). A linear fit to the Cima hawaiites only (from this study and Group 1a; Farmer et al., 1995) is shown in black. Extrapolations to low-MgO (4 wt%) and high-MgO (10 wt%) broadly overlap Cima mugearite and Pisgah/Amboy high-MgO samples, respectively.

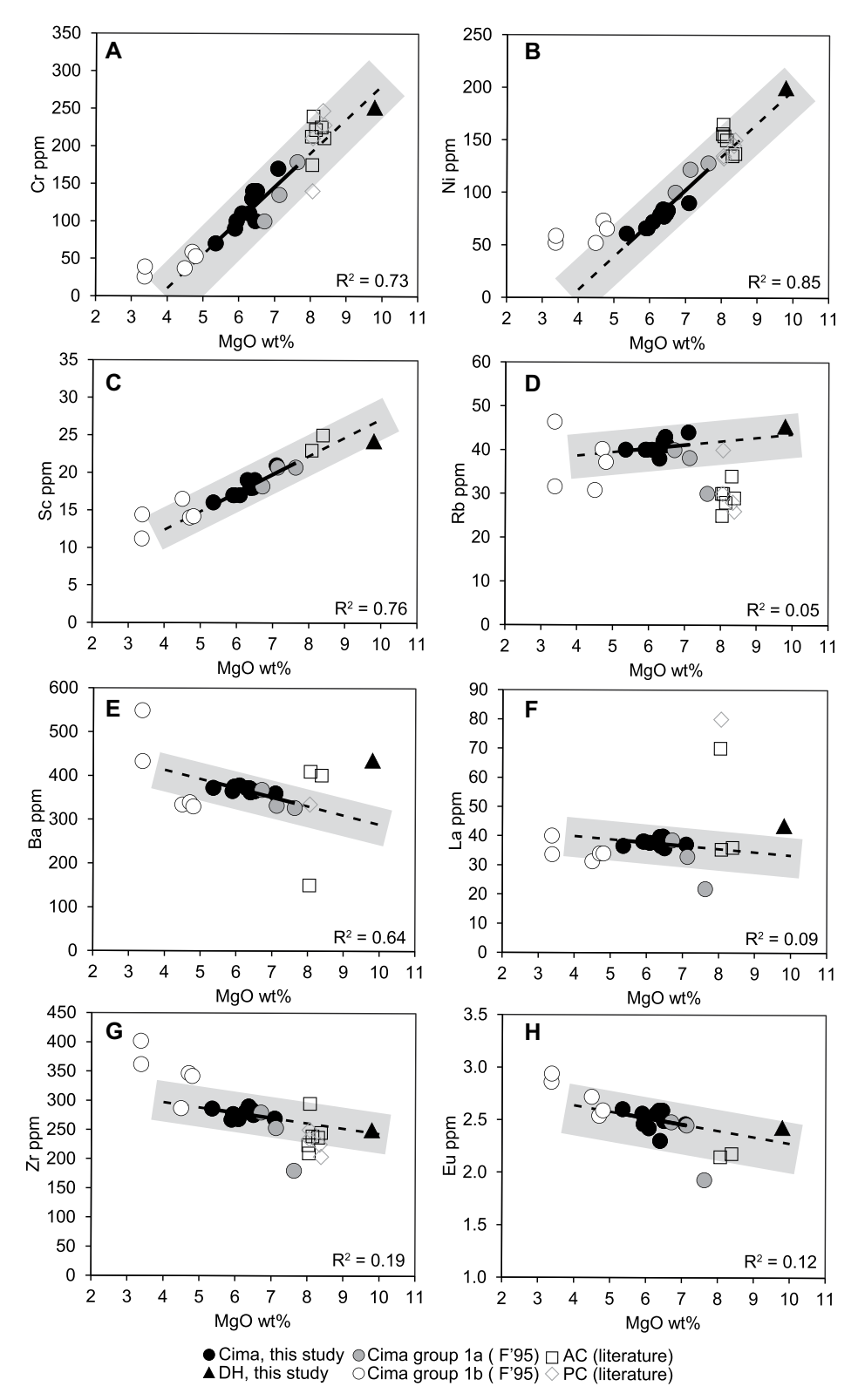


Figure 6. Whole-rock trace-element variation plots (Cr, Ni, Sc, Rb, Ba, La, Za, Eu) versus MgO (wt%) for the same samples presented in Figure 5. A similar linear fit to only the Cima hawaiite data from this study combined with the Farmer et al. (1995) Group 1a samples is shown in black. Extrapolations to low-MgO (4 wt%) and high-MgO (10 wt%) broadly overlap Cima mugearite and Pisgah/Amboy high-MgO samples, respectively.

and are fitted to a linear relationship for the top 3 mol%. This relationship is used to calculate CaO, NiO, and MnO wt% for the most Mg-rich olivine composition (Table 2), which eliminates scatter associated with microprobe analytical uncertainty.

In all Cima and Dish Hill samples, most analyzed olivine crystals contain \geq 0.2 wt% CaO. However, in nine samples (five of which have entrained mantle xenoliths), a separate and sparse population of low-CaO olivine is found. These olivine crystals have CaO contents that overlap those analyzed in olivines from Cima peridotite xenoliths $(0.10 \pm 0.03 \text{ wt}\% \text{ CaO};$ Wilshire et al., 1991) and the adjacent Dish Hill xenoliths (0.07 \pm 0.02 CaO wt%; Wilshire et al., 1991). It is well established in the literature that elevated CaO contents can be used to distinguish olivine phenocrysts from olivine xenocrysts that are disaggregates of peridotite (e.g., Simkin and Smith, 1970; Heinrich and Besch, 1992; Luhr and Aranda-Gómez, 1997; Housh et al., 2010; Brehm and Lange, 2020). Thus, the high-CaO population of olivine in each sample is interpreted to have grown as phenocrysts.

Back-scattered electron (BSE) images of the most Mg-rich olivine crystals in eight representative samples from this study are shown in Figure 11. The crystals (mostly Fo₈₆₋₈₇) are notable for their relatively thin Fe-rich rims, despite the wide variation in whole-rock MgO content. X-ray intensity maps of P and Fe for three of these eight olivine crystals (CC-1, Cima-3, Cima-8) are shown in Figure 12. Olivine phenocrysts show patterns of complex P zoning (e.g., dendritic, oscillatory) with relatively thin Fe-rich rims, especially in the sample shown that has the lowest whole-rock MgO content (6.5 wt%; Cima-8). For comparison, a P map of olivine from a San Carlos, Arizona, USA peridotite xenolith from Brehm and Lange (2020) is also shown (Fig. 12) and displays no P zonation. Thus, the presence of complex P-zonation in olivine is also evidence of phenocryst growth. BSE images of other olivine crystals from the Cima samples that range to lower Fo-contents (Fig. 13) also display diffusion-limited growth textures (e.g., skeletal and hopper).

Clinopyroxene Results

Details concerning the clinopyroxene results are presented in the supplemental file, and only key points are highlighted below. Individual spot analyses (Table S4; see footnote 1) along each crystal transect were assigned to one of three textural categories: (1) sector- or oscilla-

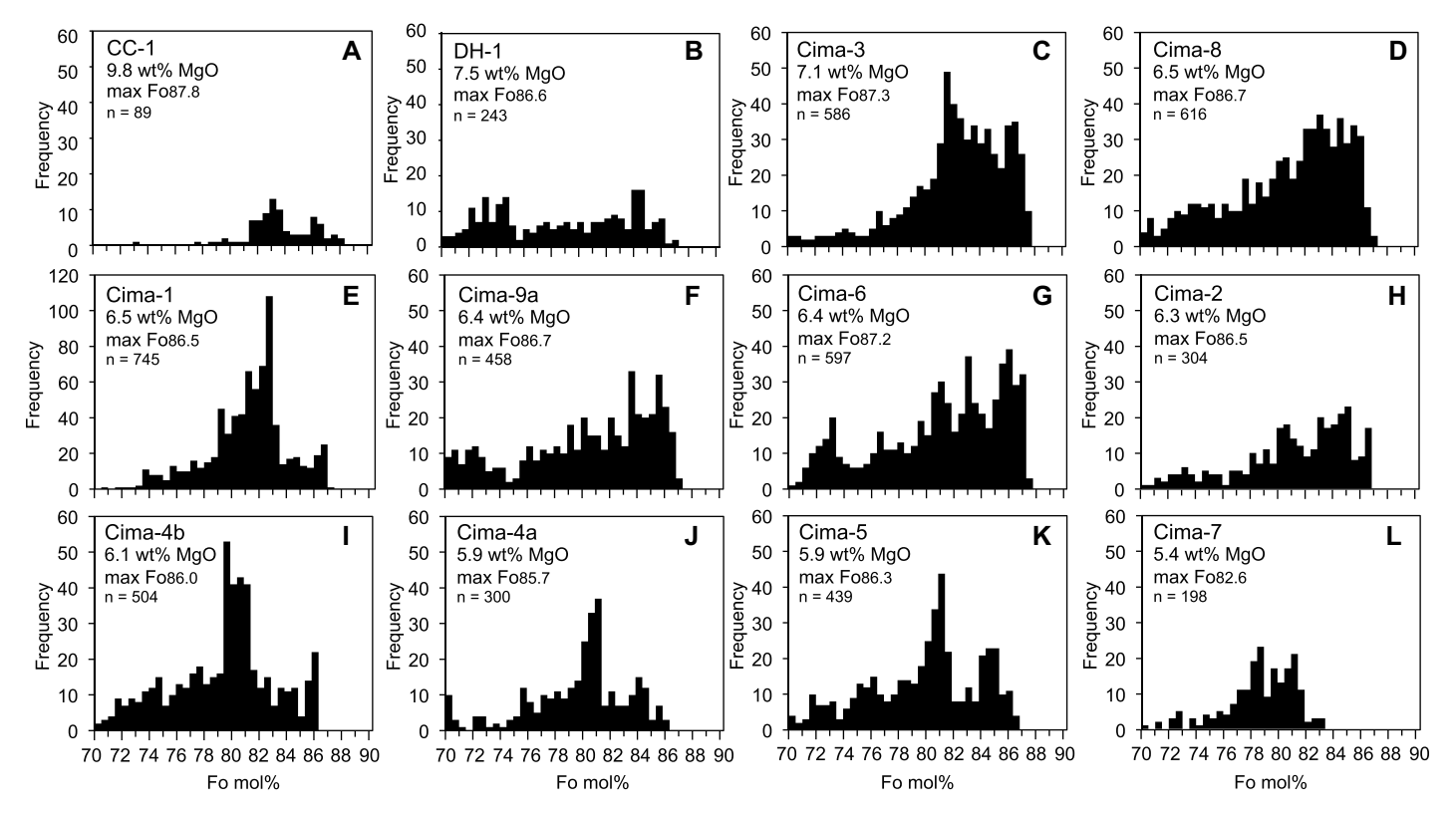


Figure 7. Histograms of Fo mol % (= $X_{MgO}/(X_{MgO} + X_{FeO}) \times 100$) for the Cima and Dish Hill samples (California, USA). The most Mg-rich olivine compositions (Table 2), whole-rock MgO wt % (Table 1), and number of analyses (n) are given for each sample.

tory-zoned, (2) vermicular (i.e., spongy), or (3) non-vermicular (i.e., non-spongy). BSE images of representative crystals from each textural category are shown in Figure S4 with some displaying multiple textures within the same crystal. In most samples, the dominant clinopyroxene texture is vermicular, which is consistent with diffusion-limited, rapid growth (e.g., Roeder et al., 2001). Non-vermicular textures are next in abundance, and in most crystals sector- or oscillatory-zonations are relatively sparse to absent (e.g., Cima-5). Cima-1 is the only sample where sector- or oscillatory-zonations dominate the clinopyroxene phenocryst population. Histograms of Mg# for the clinopyroxene analyses in each sample are given in Figure S5. Plots of wt% Na₂O, TiO₂, and Cr₂O₃ versus Mg# in each sample are shown in Figure S6. Clinopyroxene-melt barometry is applied later in the paper.

Plagioclase Results

Details concerning the plagioclase results are presented in the supplemental file, and only key points are highlighted below. Most plagioclase phenocryst analyses in Cima-8, -1, and -2 hawaiite samples range from An_{68-54} . Only sparse rim analyses below An_{50} were obtained.

Histograms of these analyses are shown in Figure S7.

Fe-Ti Oxide Results

Individual analyses of titanomagnetite from eight samples and ilmenite from six samples are reported in Table S5A (see footnote 1). Six samples (Cima-3, -4a, -4b, -5, -8, -9) were analyzed for both oxides. The Bacon and Hirschmann (1988) Mg/Mn test for equilibrium was used to evaluate all possible pairs of ilmenite and titanomagnetite in each sample that could have co-crystallized. For those oxide pairs that passed the test, the Fe-Ti two-oxide thermometer and oxybarometer of Ghiorso and Evans (2008) was applied. The results for all six samples are shown in a plot of lnfO2 versus temperature, with the quartz-fayalite-magnetite (QFM) buffer shown for reference (Fig. 14, Table S5B; see footnote 1). Calculated temperatures and ΔQFM values ($log_{10}fO_2$ relative to the quartz-fayalite-magnetite buffer) at the onset of oxide co-crystallization in each sample are presented in Table S5C (see footnote 1). Onset temperatures range from 1098 to 955 °C and Δ QFM values range from -0.3 to -1.3.

CONSTRAINTS ON CONDITIONS DURING PHENOCRYST GROWTH

Diffusion-Limited Rapid Growth Textures in Olivine and Clinopyroxene

The occurrence of peridotite xenoliths in Dish Hill and several Cima flows indicates that magma ascent through the crust was sufficiently rapid to overcome xenolith settling velocities (e.g., Sparks et al., 1977; Spera, 1980, 1984), which precludes phenocryst growth during prolonged storage in a crustal reservoir. This raises the possibility of phenocryst growth during ascent, which is consistent with diffusionlimited growth textures in olivine (e.g., skeletal and hopper; Figs. 13A-13D) and clinopyroxene (vermiform; Figs. 13E and 13F) from several Cima samples. Even in olivine crystals that do not display skeletal textures in BSE images, X-ray element maps reveal complex P zoning patterns that are consistent with diffusion-limited (i.e., rapid) crystallization (e.g., Lofgren, 1974; Milman-Barris et al., 2008; Welsch et al., 2014; Shea et al., 2019). In the case of clinopyroxene, the vermicular texture likely reflects an initial dendritic architecture that is then partially overgrown (e.g., Welsch et al., 2016). A similar texture is found in vermiform chromite crystals

TABLE 2. COMPOSITION OF THE MOST Mg-RICH OLIVINE AND THERMOMETRY RESULTS AT THE ONSET OF PHENOCRYST GROWTH

Oxide (wt%)	*CC-1	DH-1	Cima-3	*Cima-8	Cima-1	*Cima-9	Cima-6	Cima-2	*Cima-4b	*Cima-4a	*Cima-5	Cima-7
SiO ₂	41.27	40.70	40.88	41.11	40.80	41.05	40.46	41.09	40.76	40.66	40.83	40.34
Al_2O_3	0.05	0.05	0.05	0.05	0.06	0.05	0.05	0.04	0.09	0.04	0.05	0.04
FeO	11.67	12.85	12.04	12.66	12.49	12.55	12.21	12.85	13.16	13.43	13.09	16.33
†MnO	0.17	0.19	0.17	0.16	0.17	0.17	0.17	0.18	0.17	0.17	0.18	0.21
MgO	46.89	46.52	46.52	46.45	45.00	46.06	46.77	46.13	45.26	45.28	46.13	43.35
Cr₂O₃ †NiO	0.06	0.04	0.06	0.04	0.06	0.04	0.03	0.05	0.05	0.04	0.04	0.02
†Ni̇̃O ຶ	0.31	0.23	0.25	0.28	0.31	0.23	0.29	0.36	0.28	0.25	0.27	0.21
†CaO	0.23	0.22	0.23	0.24	0.24	0.24	0.24	0.25	0.22	0.22	0.22	0.22
Total	100.7	100.8	100.2	101.0	99.1	100.4	100.2	100.9	100.0	100.1	100.8	100.7
§Fo (mol%)	87.8	86.6	87.3	86.7	86.5	86.7	87.2	86.5	86.0	85.7	86.3	82.6

Olivine-melt thermometry (Pu et al., 2017)

formed during rapid crystal growth experiments on basalts (Roeder et al., 2001). Sector zoning in clinopyroxene (Fig. S4) is also indicative of rapid, diffusion-limited growth (e.g., Kouchi et al., 1983; Skulski et al., 1994; Welsch et al.,

2016). Diffusion-limited growth textures in both olivine and clinopyroxene are consistent with crystallization under an effective undercooling ($\Delta T = T_{liquidus} - T_{melt}$) (e.g., Lofgren, 1974; Welsch et al., 2014; Shea et al., 2019), which

can readily develop in mafic melts during ascent through the crust along fractures, if there is an initial kinetic delay to nucleation after melt segregation followed by rapid cooling \pm degassing (e.g., Brehm and Lange, 2020).

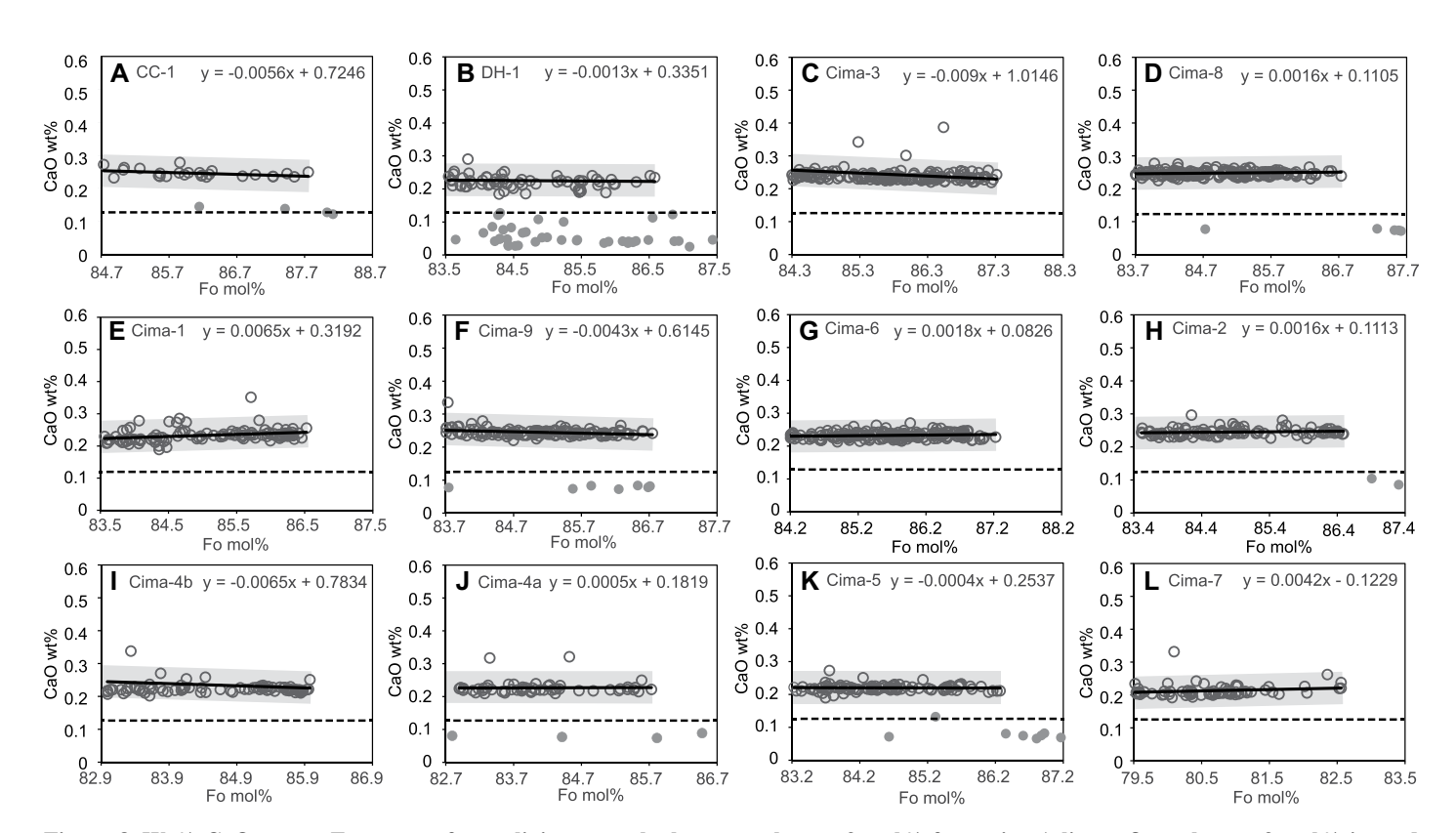


Figure 8. Wt% CaO versus Fo content from olivine crystals that span the top 3 mol% forsterite. A linear fit to the top 3 mol% is used to calculate CaO wt% for the most forsteritic olivine. The gray field is the 2σ analytical error bar derived from electron microprobe counting statistics. The range of CaO wt% measured in mantle xenolith olivine compositions from Cima $(0.10 \pm 0.03;$ Wilshire et al., 1991) and the adjacent basalt deposit at Dish Hill $(0.08 \pm 0.02 \text{ wt\%};$ Luffi et al., 2009) (California, USA) is the source of the dotted line at 0.10 wt% CaO, below which olivine analyses are interpreted as derived from mantle xenoliths. Gray dots represent individual spot analyses in olivine phenocrysts that fall within the range of CaO wt% for mantle xenolith olivine specifically from Cima/Dish Hill mantle xenoliths. They are therefore considered potential disaggregates from mantle xenoliths and are not included in the linear fit to the top 3 mol% Fo.

 $[\]begin{array}{ll} \mbox{"T_{Mg} (°C)$} & 1247 \pm 4 \\ \mbox{"T_{Ni} (°C)$} & 1196 \pm 15 \\ \mbox{"$\Delta T = T_{Mg} - T_{Ni}$ (°C)$} & 52 \pm 15 \\ \mbox{$D_{Ca}$} & 0.021 \\ \end{array}$

^{*}Xenolith bearing samples.

[†]MnO, NiO, and ČaO wt% from linear fits in Figures 7, 8, and 9, respectively.

 $Fo \text{ mol} = X_{MgO}/(X_{MgO} + X_{FeO}) \times 100.$

 $^{^{\#}}T_{Mg}$, T_{Nj} , and $\overset{\text{mag}}{\Delta T}$ calculated according to the model of Pu et al. (2017); errors propagated from analytical uncertainty. T—temperature.

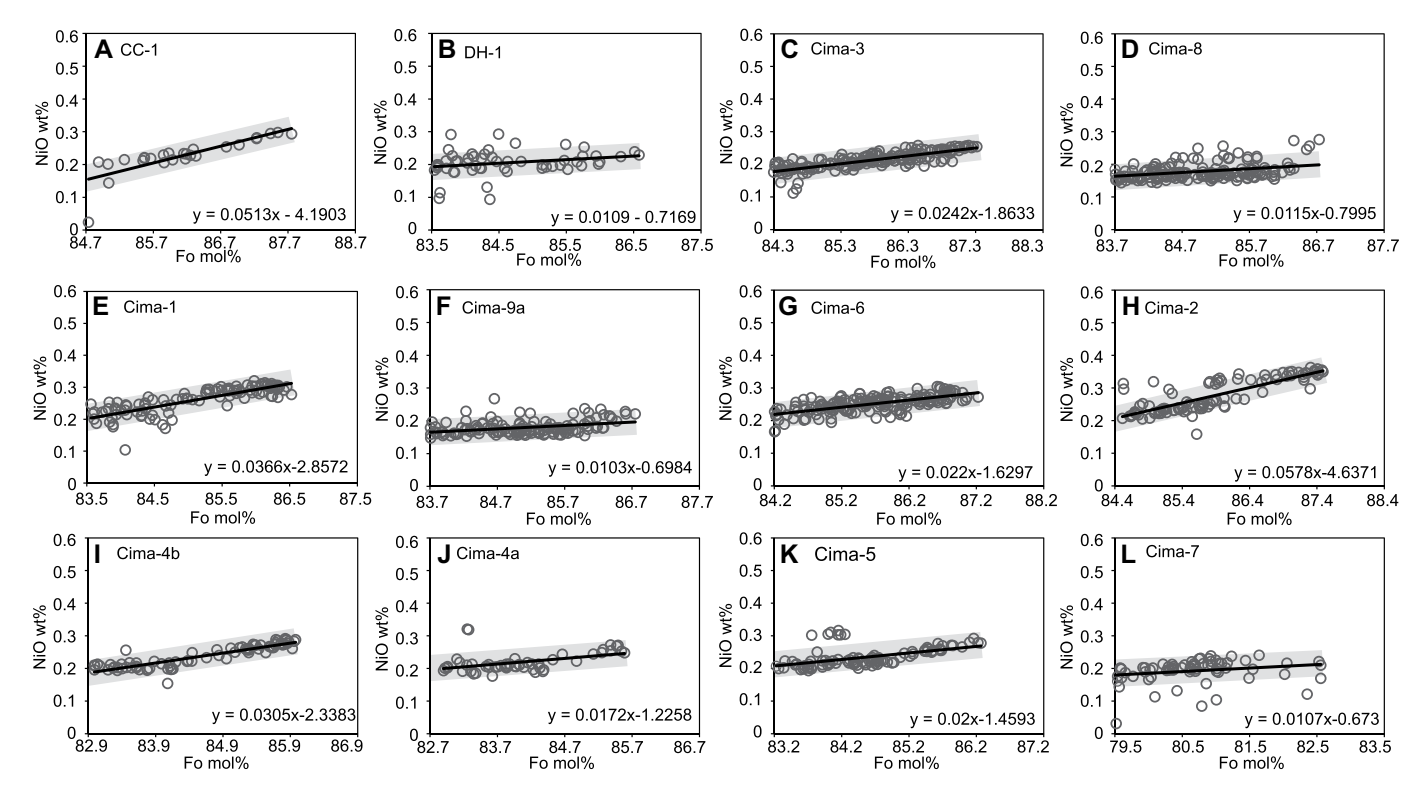


Figure 9. Wt% NiO versus Fo content from olivine within the top 3 mol% Fo in each of the Cima and Dish Hill basalts (California, USA). A linear fit to the top 3 mol% is shown in and is used to calculate NiO wt% for the most Mg-rich olivine composition. The gray field is the 2σ analytical error bar derived from electron microprobe counting statistics.

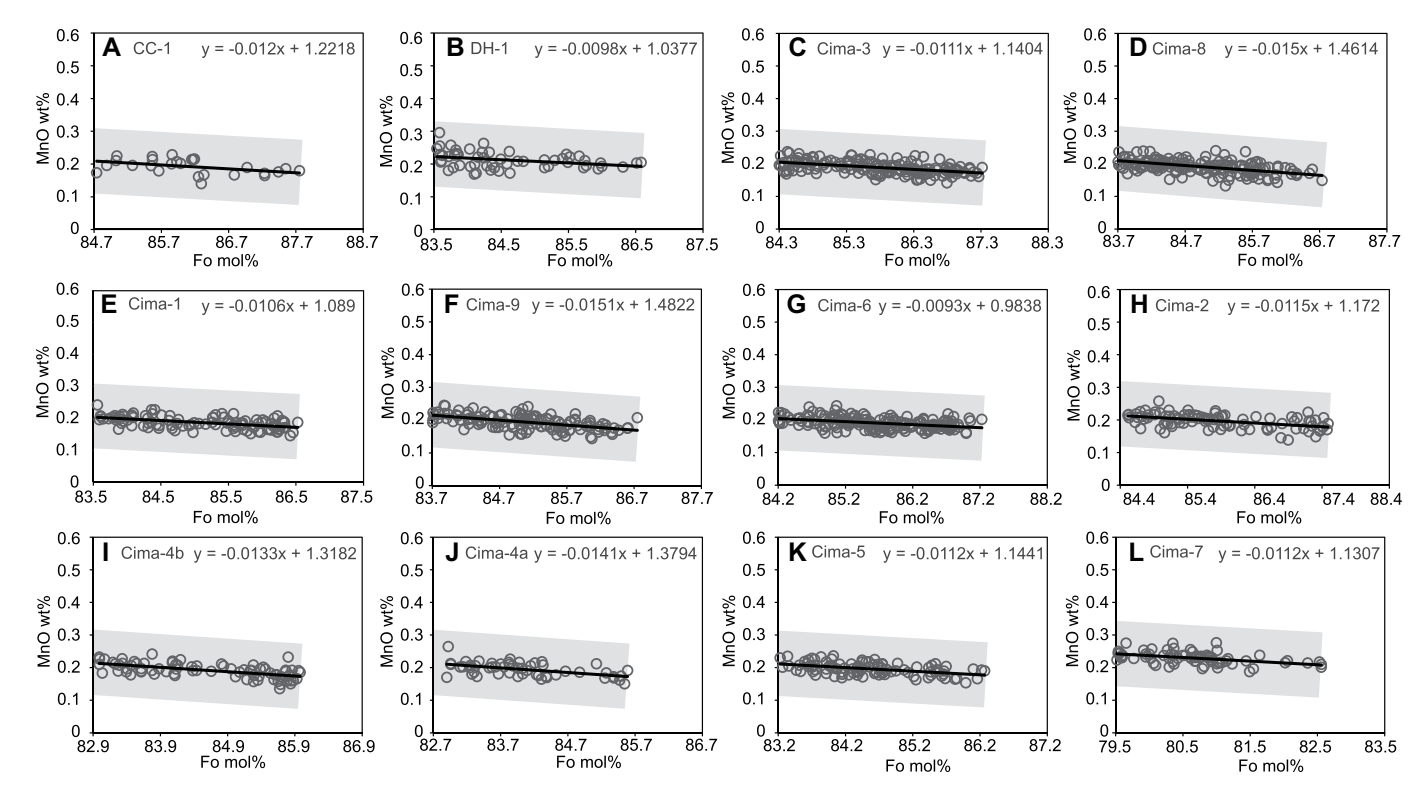


Figure 10. Wt% MnO versus Fo content from olivine crystals within the top 3 mol% Fo in each of the Cima and Dish Hill basalts (California, USA). A linear fit to the top 3 mol% is shown in and is used to calculate MnO wt% for the most Mg-rich olivine compositions. The gray field is the 2σ analytical error bar derived from electron microprobe counting statistics.

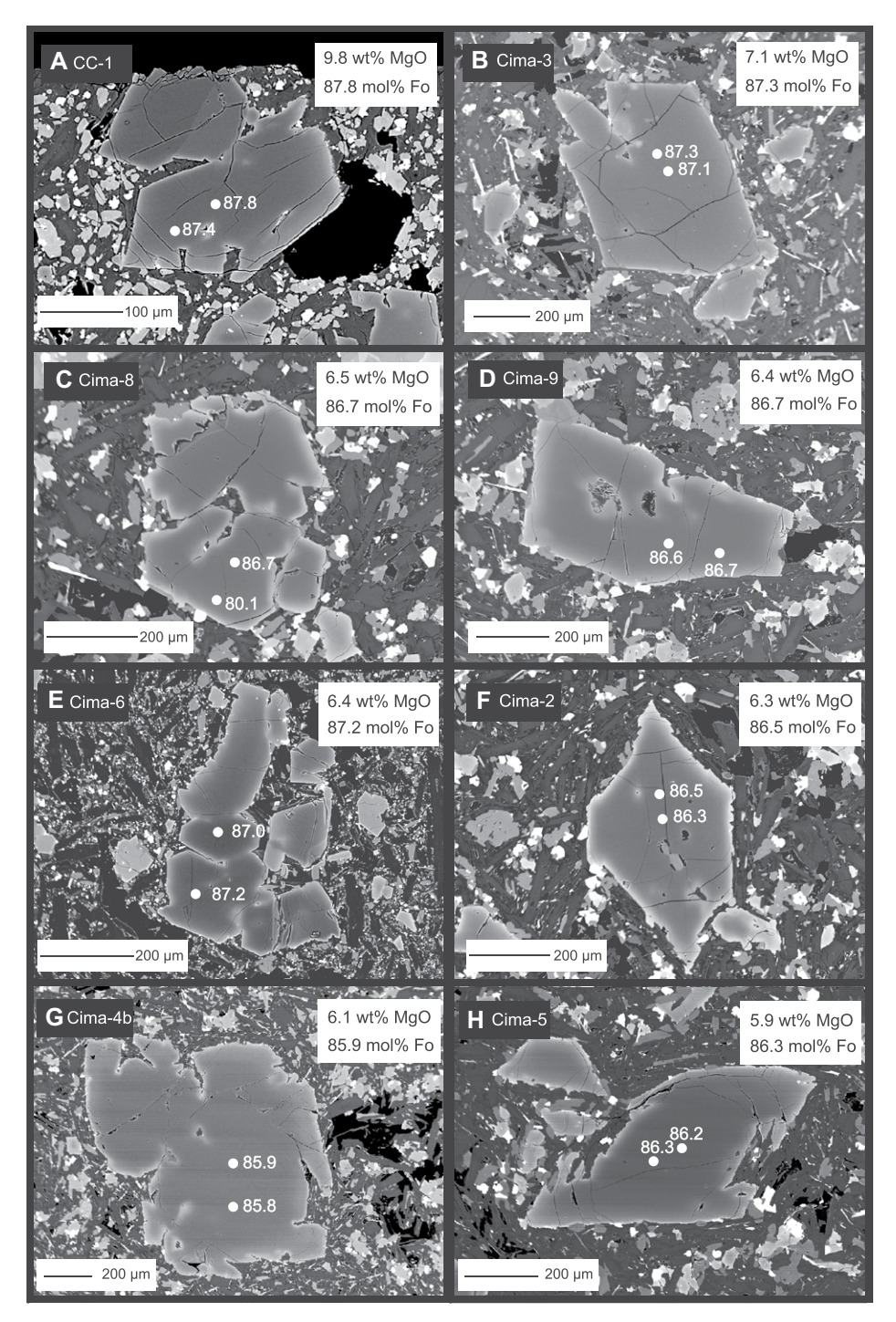


Figure 11. Representative back-scattered electron images of the most Mg-rich olivine composition from eight samples from the Cima volcanic field, California, USA. Representative individual spot analyses (mol% Fo) for each crystal are shown in yellow. All crystals show thin Fe-rich rims, consistent with a short time interval between magma mixing and eruption.

$\begin{aligned} & Application \ of \ the \ ^{Fe2+\text{-}Mg}K_D(olivine\text{-}melt) \\ & Equilibrium \ Test \ at \ the \ Liquidus \end{aligned}$

If the hypothesis of phenocryst growth during ascent is viable, it is possible that the first olivine to grow during ascent (i.e., composition at the liquidus) is preserved in erupted samples, due to insufficient time for re-equilibration during continued crystallization. The best test of olivinemelt equilibrium at the liquidus is to use the $^{\rm Fe2+-}$ $^{\rm Mg}K_{\rm D}({\rm olivine-melt})$ exchange coefficient, which has been well calibrated in the literature for a

range of melt compositions (e.g., Gee and Sack, 1988; Toplis, 2005; Putirka, 2016). Because the exchange reaction involves Fe $^{2+}$, the Fe $^{3+}/\text{Fe}^{T}$ ratio in the melt must be known. In this study, a redox state of $\sim\!\Delta\text{QFM}=0$ is used for all samples based on the Fe-Ti oxide results. This leads to a calculated Fe $^{3+}/\text{Fe}^{T}$ ratio of $\sim\!0.16$ using the model of Kress and Carmichael (1991), which was used to be consistent with the software MELTS (Ghiorso and Sack, 1995; Asimow and Ghiorso, 1998). Plank and Forsyth (2016) report similar Fe $^{3+}/\text{Fe}^{T}$ ratios of 0.17 for Cima olivine-hosted melt inclusions, based on fO_2 constraints derived from V-partitioning data and application of the Kress and Carmichael (1991) model.

To perform this equilibrium test, the most Mg-rich olivine phenocryst analyzed in each sample is plotted as a function of the whole-rock Mg# (using $Fe^{3+}/Fe^T=0.16$) in Figure 15. Superimposed on this plot are isopleths of $^{Fe2+-}MgK_D$ (olivine-liquid) values:

$$F_{e^{2+}-Mg}K_{D}\left(olivine-liquid\right) = \left(\frac{X_{Fe^{2+}O}}{X_{MgO}}\right)^{oliv}$$

$$\left(\frac{X_{MgO}}{X_{Fe^{2+}O}}\right)^{liquid} \tag{1}$$

The results for individual samples (Fig. 15) are compared to predicted values from MELTS (Ghiorso and Sack, 1995; Asimow and Ghiorso, 1998) and those calculated using the models of Gee and Sack (1988), Toplis (2005), and Putirka (2016) in Table 3A. The results show that all samples but one (Dish Hill CC-1) fail the test, with inferred Fe2+-MgK_D(olivine-melt) values of \sim 0.18–0.22, which are far too low for equilibrium. In other words, the most Mg-rich olivine phenocryst analyzed in each sample is too Mg-rich to be in equilibrium with the wholerock liquid composition. Only the high-MgO (9.8 wt%) basanite from Dish Hill (CC-1) has a $^{\text{Fe2+-Mg}}K_{D}(\text{olivine-melt})$ value $({\sim}0.28)$ that approaches equilibrium conditions (Table 3A).

A similar suite of intraplate hawaiite lavas in western Mexico (the Sangangüey suite; Nelson and Carmichael, 1984) also contain olivine phenocrysts that are too Mg-rich to be in equilibrium with their host lavas (Díaz-Bravo et al., 2014; Mesa and Lange, 2021). The disequilibrium olivine crystals (too Mg-rich) in these two suites of intraplate hawaiites (Cima and Sangangüey) are in stark contrast to what has been documented for basalts derived from subduction-modified lithosphere in eastern California (i.e., the Big Pine and Long Valley volcanic fields; Brehm and Lange, 2020; Jolles and Lange, 2021), as well as basalts from the active Mexican arc (i.e., the Tancítaro volcanic field; Pu

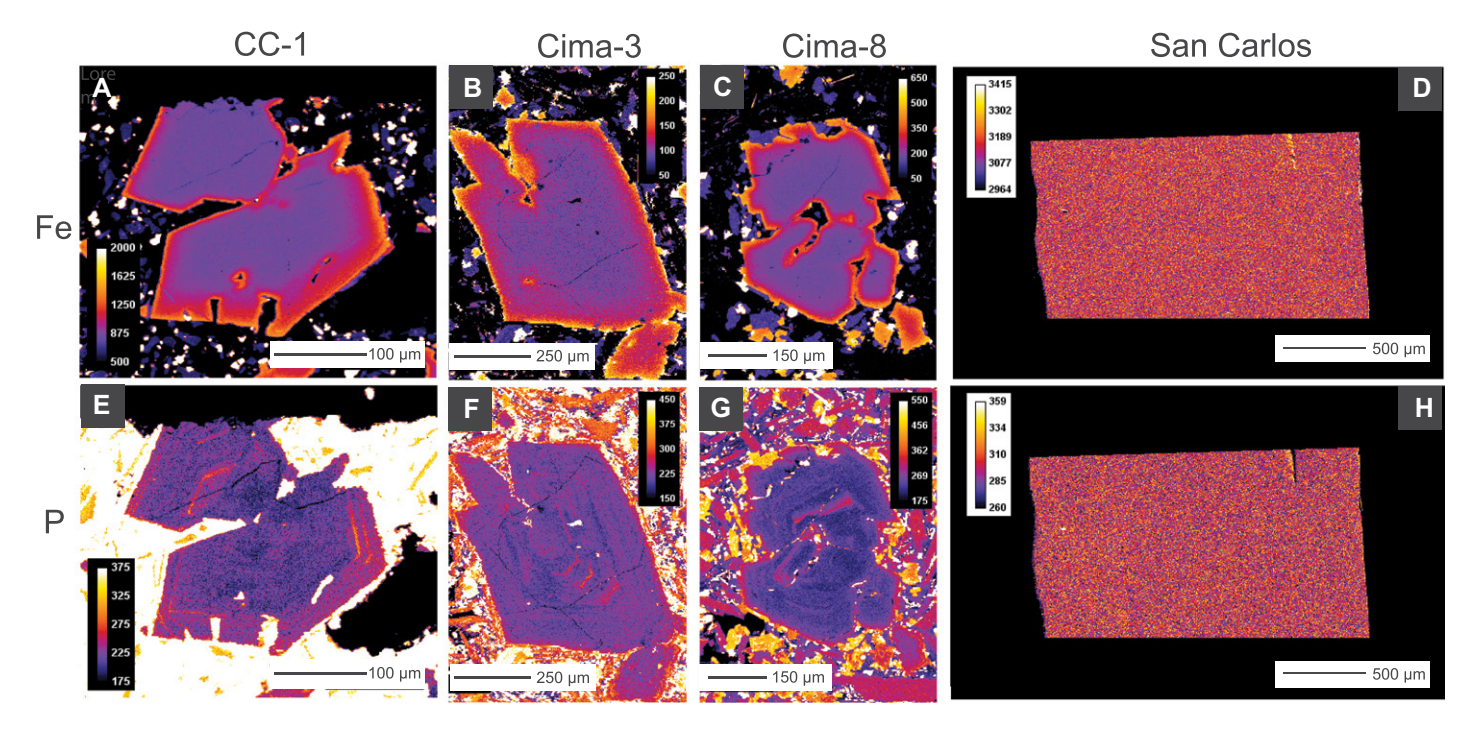


Figure 12. X-ray intensity maps of Fe (top) and P (bottom) for the most Mg-rich olivine analyzed in three samples from the Cima volcanic field, California, USA. P zoning patterns in olivine are consistent with an initial period of diffusion-limited rapid growth (e.g., Milman-Barris et al., 2008; Welsch et al., 2012; 2014; Shea et al., 2019). Shown for comparison are X-ray intensity maps of P and Fe from a San Carlos, Arizona, USA peridotite xenolith from Brehm and Lange (2020), which shows no P zoning.

et al., 2017). In these three studies, the most Mgrich olivine in each of 36 of 37 samples passes the olivine-liquidus equilibrium test when paired with their respective whole-rock sample composition, as illustrated in Figure 15. For these three volcanic fields, a melt Fe^{3+}/Fe^{T} ratio of 0.24 was employed (directly measured by μ -XANES analyses of olivine-hosted melt inclusions in Big Pine basalts; Kelley and Cottrell, 2012).

The results for the Big Pine, Long Valley, and Mexican arc samples (Tancítaro volcanic field, TVF) in Figure 15 overlap Fe2+-MgKD(olivinemelt) isopleths predicted by models from the literature (summarized in Brehm and Lange, 2020). This supports the hypothesis that the basalts from all three volcanic fields grew their olivine phenocrysts rapidly during ascent and that the most Mg-rich olivine analyzed in each sample closely represents the liquidus olivine for a melt with the whole-rock sample composition. This enabled application of the Pu et al. (2017) olivine-melt thermometer and hygrometer to this pairing (most Mg-rich olivine and melt with whole-rock composition) to all 36 samples from the Big Pine, Long Valley, and TVF (Mexican arc) volcanic fields to obtain temperature and water content at the liquidus (Pu et al., 2017; Brehm and Lange, 2020; Jolles and Lange, 2021). In this study, a similar approach was taken, but only for the single sample (Dish Hill CC-1) that passed the olivine-melt equilibrium liquidus test.

Olivine-Melt Thermometry

Most olivine-melt thermometers in the literature are based on the partitioning of Mg between olivine and the melt ($D_{Mg}^{\text{oliv/liq}}$), and yet $D_{Mg}^{\text{oliv/liq}}$ is strongly sensitive to dissolved H₂O in the melt (e.g., Almeev et al., 2007; Médard and Grove, 2008). This requires that H₂O contents be known before Mg-based olivine-melt thermometers that include corrections (e.g., Putirka et al., 2007) can be applied. In contrast, olivine-melt thermometers based on D_{Ni} oliv/liq are independent of melt water contents and require no corrections at crustal pressures (<1 GPa; Pu et al., 2017, 2021). Because the Ni-thermometer is independent of dissolved water, it provides the actual temperature at the onset of olivine crystallization (Pu et al., 2021). Moreover, because the olivine liquidus is suppressed to lower temperatures under hydrous conditions (e.g., Almeev et al., 2007; Médard and Grove, 2008), calculated T_{Ni} values are expected to be consistently lower than T_{Mg} values in hydrous basalts (Pu et al., 2017; 2021). Importantly, the magnitude of the temperature difference (i.e., $\Delta T = T_{M\sigma} - T_{Ni}$), namely the extent to which the olivine liquidus temperature is depressed, scales with the amount

of water in the melt (e.g., Pu et al., 2017, 2021; Brehm and Lange, 2020).

For the Dish Hill basanite from this study, which passed the olivine-melt equilibrium liquidus test (CC-1), the Mg- and Ni-thermometers of Pu et al. (2017) were used to calculate temperature at the onset of phenocryst growth. Values of $D_{Mg}^{\ oliv/liq}$ and $D_{Ni}^{\ oliv/liq}$ were constructed from the most Mg-rich olivine analyzed in this sample (Table 2) paired with a liquid of its whole-rock composition (Table 1). Calculated T_{Mg} and T_{Ni} are 1247 and 1196 °C, respectively. Analytical errors in $D_{Mg}^{\ oliv/liq}$ and $D_{Ni}^{\ oliv/liq}$, derived from uncertainties in the microprobe analyses and whole-rock compositions, are $\sim\!1\%$ and $\sim\!7\%$, respectively, leading to propagated 1σ uncertainties in T_{Mg} and T_{Ni} of ± 4 and ± 15 °C, respectively. Thus, ΔT (= $T_{Mg}\!-\!T_{Ni}$) is $51(\pm 16)$ °C.

Note that application of olivine-melt thermometry to other olivine phenocrysts in the hawaitte samples (e.g., peak Fo_{80-82} in several samples; Fig. 7) was not undertaken in this study. This peak Fo_{80-82} population likely grew after crystallization of other mineral phases (e.g., olivine \pm clinopyroxene \pm plagioclase \pm Fe-Ti oxides) and requires that the Ni content in the coexisting liquid at the time of peak olivine growth (e.g., Fo_{80-82}) be calculated after accounting for the effects of this multi-phase mineral crystallization. This

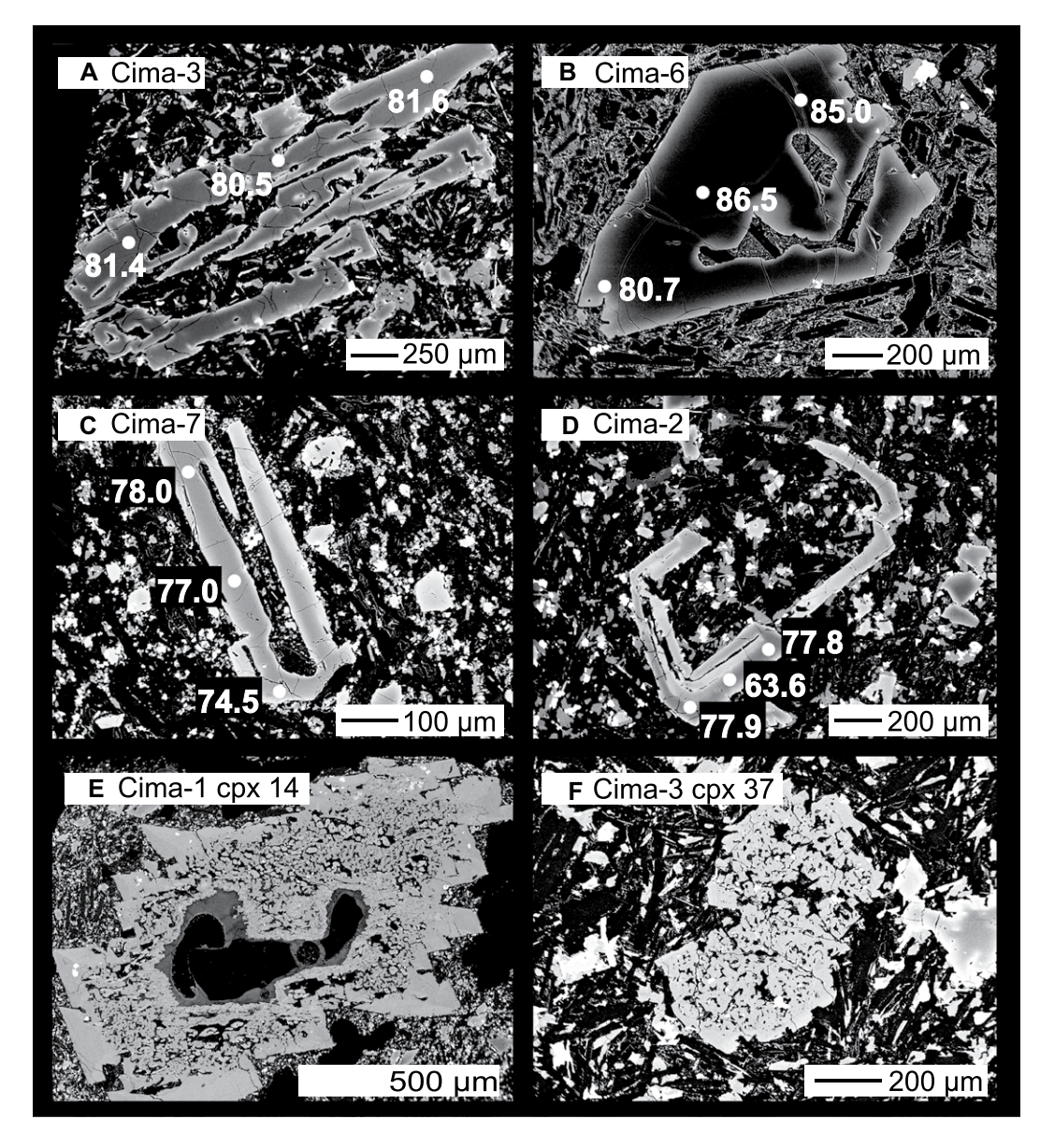


Figure 13. Representative back-scattered electron images of phenocrysts in Cima basalts (California, USA) that display diffusion-limited growth textures. (A–D) Olivine phenocrysts with hopper and skeletal textures. (E and F) Clinopyroxene phenocrysts with vermiform textures. Representative spot analyses and associated Fo contents are shown for all olivine phenocrysts.

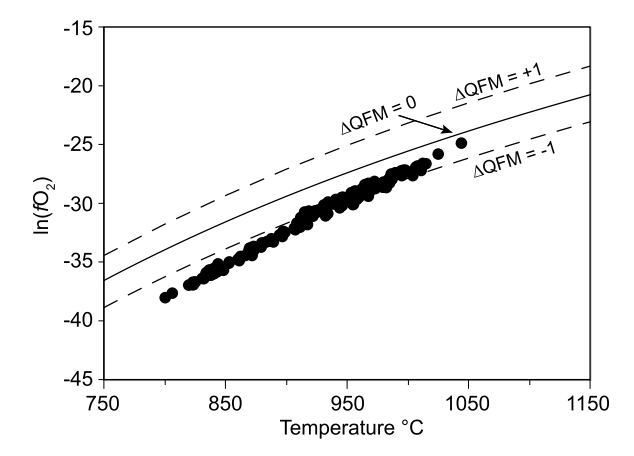
involves significant guesswork and does not result in accurate or precise knowledge of melt Ni contents, which leads to significantly large errors in $D_{Ni}^{\text{oliv/liq}}$ and thus T_{Ni} values. Therefore, Ni-based olivine-melt thermometry is only applied in this study to olivine when

Figure 14. Results for the application of Fe-Ti oxide thermometry and oxybarometry (Ghiorso and Evans, 2008) in six Cima hawaiites (California, USA) are summarized in a plot of $\ln fO_2$ versus temperature (°C) for all possible pairs of Fe-Ti oxides that pass the Bacon and Hirschmann (1988) test for equilibrium (Table S5; see text footnote 1). The location of the quartz-fayalite-magnetite (QFM) buffer is shown for reference.

it passes equilibrium liquidus tests for wholerock compositions.

Additional Test of Olivine-Melt Equilibrium at the Liquidus

With temperature in hand (i.e., T_{Ni}), an additional test of olivine-melt equilibrium at the liquidus can be made with the lattice strain model of Blundy et al. (2020), which predicts the value of $^{Mg-Mn}K_D$ (olivine-melt) on the basis of temperature and olivine composition. The advantage of this test is that it is independent of melt oxidation state and only weakly dependent on temperature (a change of 50 °C changes the K_D value by \sim 0.01). When the T_{Ni} values (Table 2; Table S7; see footnote 1) are combined with the most Fo-rich olivine analyzed in each sample (Table 2), calculated values of $^{Mg-Mn}K_D$ (olivine-



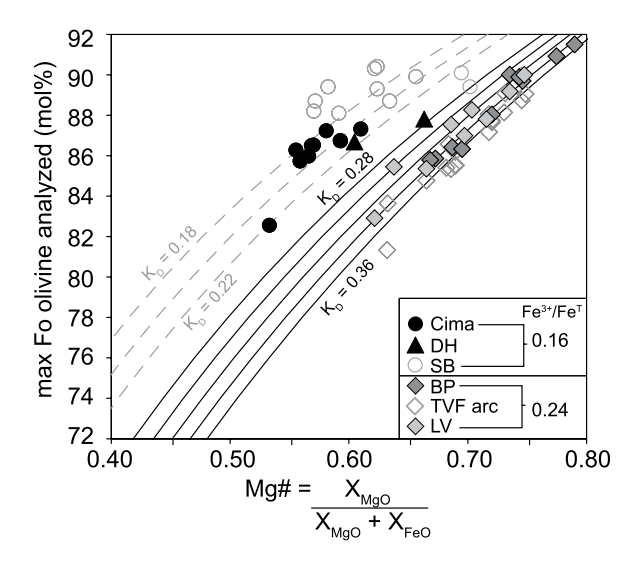


Figure 15. Plot of the most forsteritic olivine (Fo mol%) analyzed in each of the Cima and Dish Hill (DH) samples (California, USA) versus wholerock Mg# (calculated using $Fe^{3+}/Fe^{T} = 0.16$ from Fe-Ti oxides). Individual isopleths of ${}^{Fe2+\text{-Mg}}K_D$ (olivine-melt) are superimposed. For comparison, basalts from the Big Pine (BP) volcanic field (Brehm and Lange, 2020), Long Valley (LV, Jolles and Lange, 2021), the (Tancítaro volcanic field, TVF) Mexican arc (Pu et al., 2017), and the Sangangüey (SB) intraplate basalts of western Mexico (Mesa and Lange, 2021)

are shown. Whole-rock Mg# values for the BP, LV, and TVF basalts are calculated using $Fe^{3+}/Fe^{T}=0.24$ (average of μ -XANES analyses for BP, Kelley and Cottrell, 2012) and $Fe^{3+}/Fe^{T}=0.16$ for the Sangangüey basalts (Mesa and Lange, 2021).

melt) derived from the Blundy et al. (2020) model are obtained (Table 3B). These values can be compared to analyzed values of Mg-MnK_D(olivine-melt) based on the data given in Tables 1 and 2. Within a combined uncertainty of < 0.04 (strain model calculation and analyzed value), there is excellent agreement for the Dish Hill CC-1 sample, which also passes the Fe2+-MgK_D(olivine-melt) liquidus test (Table 3A; Fig. 15). This result also shows internal consistency with application of the Ni-thermometer of Pu et al. (2017; 2021). All the remaining samples fail the Mg-MnK_D(olivine-melt) test, with differences of >0.04 between analyzed values (this study; Table 3B) and those calculated from the model of Blundy et al. (2020).

Olivine-Melt Hygrometry

Previous studies (Pu et al., 2017, 2021; Brehm and Lange, 2020) have shown that the difference between T_{Mg} and T_{Ni} (i.e., $\Delta T = T_{Mg} - T_{Ni}$), when applied to samples that pass the olivine-melt equilibrium liquidus test, reflects the magnitude of the depression of the olivine liquidus due to dissolved water in the melt. As a consequence, the experimentally calibrated model of Médard and Grove (2008), which relates ΔT with dissolved water in the melt, can be used to calculate the water concentration in the Dish Hill basanite for which $T_{\rm Mg}$ and $T_{\rm Ni}$ values were obtained. The ΔT value (= T_{Mg} - T_{Ni}) of 51 (±16) °C leads to an estimated melt water content of $\sim 1.4 \, (\pm 0.5)$ wt%. This overlaps the highest H₂O content directly analyzed in olivine-hosted melt inclusions from Cima samples (≤1.35 wt%; Plank and Forsyth, 2016). An additional assessment of melt H₂O contents in CC-1 is made through the application of the Putirka et al. (2007) Mgbased olivine-melt thermometer, which includes a correction for dissolved H₂O content. In the absence of the H₂O correction, the application of the Putirka et al. (2007) model to CC-1 leads to a calculated Mg-temperature (1257 °C) that closely matches that obtained by the Pu et al. (2017) Mg-thermometer (1247 \pm 4). When melt H_2O contents of 1.4 (± 0.5) wt%, consistent with direct measurements of olivine-hosted melt inclusions (Plank and Forsyth, 2016), are used in the Putirka et al. (2007) model, the calculated temperature for CC-1 is $1226 (\pm 11)$ °C. This is within error of the calculated temperature obtained using the Ni-thermometer (1196 \pm 15).

Another parameter that is sensitive to dissolved water in the melt is D_{Ca}oliv/liq, which decreases with increasing melt water content, and has the potential to be used as an olivinemelt hygrometer (Gavrilenko et al., 2016). Brehm and Lange (2020) showed that when the average ΔT (= T_{Mg} - T_{Ni}) for three different volcanic suites is plotted against their average $D_{\text{Ca}}^{\ \text{oliv/liq}}$ values (obtained at the liquidus), a strong inverse linear correlation ($R^2 = 0.99$) is found (Fig. 16). The lowest D_{Ca} oliv/liq values correspond to the Mexican arc basalts from Pu et al. (2017), which are the most hydrous (<5.7 wt% H₂O in olivine-hosted melt inclusions; Johnson et al., 2009). Mid-ocean ridge basalts (~0.1 wt% H₂O) from Allan et al. (1989) have the highest D_{Ca}oliv/liq values, whereas the Big Pine basalts from Brehm and Lange (2020) have intermediate D_{Ca}oliv/liq values that fall between those for the Mexican arc and mid-ocean ridge basalts (MORBs) (Fig. 16). These intermediate values are consistent with published water contents from analyses of olivine-hosted melt inclusions (1.5–3.0 wt%; Gazel et al., 2012).

In this study, the value of $D_{\text{Ca}}^{\text{oliv/liq}}$ (= 0.0211) obtained for the Dish Hill basanite (CC-1) plots between the Big Pine basalts and MORBs, which is consistent with measured H₂O contents of \leq 1.4 wt% (Plank and Forsyth, 2016). A similar application of the Pu et al. (2017) olivinemelt thermometer and hygrometer to two intraplate basalts from western Mexico (Sangangüey basalts), which pass the olivine-melt equilibrium test, give results that are close to those for Dish Hill (Mesa and Lange, 2021; Fig. 16).

CALCULATED MINIMUM ASCENT VELOCITY FOR PERIDOTITE-BEARING DISH HILL BASANITE

With a liquidus temperature ($T_{Ni} = 1196$ °C) and water content (1.4 wt%) obtained for the high-MgO, peridotite-bearing Dish Hill basanite (CC-1), the viscosity and density of the melt can be calculated, enabling an estimate of its minimum ascent velocity (i.e., xenolith settling rate) at the onset of phenocryst growth using Stoke's Law:

$$v = \frac{2gr^2(\rho_{xenolith} - \rho_{liquid})}{9\eta}$$
 (2)

In Equation 2, g is the gravitational acceleration (9.8 ms⁻²), r is the radius of the mantle xenolith (m), ρ is density (g/cm⁻³) of xenolith and basanite liquid, and η is the viscosity of the basanite liquid (Pa s). As noted by Sparks et al. (1977), this calculation can only be applied to Newtonian fluids, namely basaltic melts prior to crystal growth. As crystallization proceeds, the magma will transition to a Bingham fluid (by \sim 13% crystallization; Ishibashi and Sato, 2010), and Stoke's Law is no longer applicable. Therefore, Stoke's Law can be applied to the Dish Hill basanite after melt segregation from the mantle, at the onset of crystallization at the liquidus.

To calculate the minimum ascent velocity, the melt composition of CC-1 (Dish Hill) was used for calculation of melt density and viscosity, assuming a dissolved water content of $\sim\!1.4$ wt% and liquidus temperature of 1196 °C. The models of Lange and Carmichael (1990), Lange (1996), and Ochs and Lange (1999) were used to calculate melt density (2.67 g/cm³) at 0.5 GPa (based on maximum volatile saturation pressure of $\sim\!0.45$ GPa from melt inclusion data on Cima samples from Plank and Forsyth, 2016). The effect of up to $\sim\!1$ wt% CO2 dissolved in the melt, prior to CO2 degassing (Plank and Forsyth,

		TABLE 3A. FE2+-MGK	FE2+-MGKD(OLIV-	·MELT) TEST A	(OLIV-MELT) TEST AT LIQUIDUS COMPARED TO PREDICTED VALUES FROM LITERATURE	MPARED TO F	PREDICTED VA	LUES FROM L	ITERATURE			
Calc. Fe2+-MgK _D (oliv-melt)	CC-1	DH-1	Cima-3	Cima-8	Cima-1	Cima-9	Cima-6	Cima-2	Cima-4b	Cima-4a	Cima-5	Cima-7
*MELTS (AQFM = 0)	0.27	0.27	0:30	0:30	0.29	0:30	0.29	0:30	0.30	0.29	0.29	0.29
+Toplis (2005)	0.27	0.27	0.28	0.27	0.26	0.28	0.27	0.27	0.27	0.27	0.27	0.27
§Putirka (2016)	0.32	0.32	0.33	0.33	0.32	0.33	0.33	0.33	0.33	0.33	0.33	0.33
Average \pm 1 $^{\sigma}$	0.29 ± 0.03	$0.29 \pm 0.03 0.29 \pm 0.03 0.30 \pm 0.02$	$\boldsymbol{0.30 \pm 0.02}$	0.30 ± 0.03	$\textbf{0.29} \pm \textbf{0.03}$	$\boldsymbol{0.30 \pm 0.02}$	$\boldsymbol{0.30 \pm 0.03}$	0.30 ± 0.03	0.30 ± 0.03	$\boldsymbol{0.30 \pm 0.03}$	0.30 ± 0.03	$\textbf{0.29} \pm \textbf{0.03}$
#This study	0.28	0.24	0.23	0.22	0.21	0.22	0.20	0.21	0.21	0.21	0.20	0.24
Model average-this study	0.01	0.05	0.08	0.08	0.08	0.08	60.0	60.0	60.0	0.09	0.10	0.05
Pass/Fail	Pass	Fail	Fail	Fail	Fail	Fail	Fail	Fail	Fail	Fail	Fail	Fail

from the software MELTS the ($\Delta QFM = 0$, anhydrous; Ghiorso and Sack, 1995; Asimow and Ghiorso, 1998) c. of Fe2+MgK_D(oliv-melt) fr c. of Fe2+MgK_D(oliv-melt) fr c. of Fe2+MgK_D(oliv-melt) fr ic. of Fe2+MgK_D(oliv-melt) s ic. of Fe2+MgK_D(oliv-melt) s

from Toplis (2005). Calculated at anhydrous conditions at $\Delta QFM = 0$. from Putirka (2016) using their Equation 8c. at the liquidus using data from Tables 1 and 2 and a melt $Fe^{3+}/Fe^{T} = 0.16$.

	L	ZINM-SW C	NAMES AND THE TAXABLE TO THE TAXABLE OF THE TAXABLE			. כום כד			L			
	IABLE 35	J ™.N _D (OL	IV-IVIELI) IES I	AI LIGOIDO	SCOMPAREL	טוטפאייטטו	I ED VALUES	THOM IT INCH	AI ORE			
Calc. Mg-MnK _D (oliv-melt)	CC-1	DH-1	Cima-3	Cima-8	Cima-1	Cima-9	Cima-6	Cima-2	Cima-4b	Cima-4a	Cima-5	Cima-7
*Blundv et al. (2020) @T _{Ni}	0.216	0.222	0.197	0.192	0.184	0.199	0.190	0.179	0.187	0.190	0.186	0.201
†This study	0.199	0.162	0.155	0.131	0.136	0.141	0.137	0.134	0.139	0.133	0.132	0.146
Blundy '2020—this study	0.018	0.059	0.042	0.062	0.048	0.058	0.052	0.045	0.049	0.057	0.054	0.054
SDace/Eail	Dace	<u></u>	<u>:</u>	ΞĊ	: <u>-</u>	<u>.</u>	ie i	<u>:</u>	<u>:</u>	iou	icu	ie L

Equation 10) and either T_{Ni} or T_{Mq} (this study) Notes: oliv—olivine; QFM—quartz-fayalite-magnetite; Calc.—calculation. *Calc. of Mg-MmK_D(oliv-melt) using Blundy et al. (2020, Equation 10) and ei *Calc. of Mg-MmK_D(oliv-melt) at the liquidus using data from Tables 1 and 2

liquidus test if measured values are within ± 0.04 of predicted model values (Blundy et al.,

2020)

2016), only slightly reduces the melt density to \sim 2.66 g/cm³ at 1196 °C and 0.5 GPa. The model of Hui and Zhang (2007) was used to calculate melt viscosity (~9.1 Pa s) at 1196 °C and 1.4 wt% H_2O . The effect of ~ 1 wt% dissolved CO₂ on the viscosity of the basanite melt at this temperature is negligible (e.g., Kleest and Webb, 2021). A wide range of diameters (5-20 cm) have been reported for the Dish Hill xenoliths. Therefore, calculations were made for the two endmember sizes (i.e., radii of 2.5 and 10 cm). Mantle xenoliths from the Cima volcanic field are lherzolites with an average density of 3.2 gcm⁻³ (Wilshire et al., 1988) and are used as an estimate of xenolith density for the adjacent Dish Hill basalts. With these input parameters, minimum ascent velocities at the onset of crystallization range from 0.08 to 1.35 m/s (\sim 0.3 to ~4.9 km/h) for samples carrying xenoliths that range from 5 to 20 cm in diameter, respectively. At these ascent velocities, the basanite melts could have traversed the crustal column beneath the Mojave Desert (~36 km; Plank and Forsyth, 2016) within <119-7 h. The range of dike widths (w) for these ascent velocities (velocity = $g\Delta\rho w^2/12\eta$; Petford et al., 1993), assuming an average crustal density of ~ 2.85 g/cm³, is > 7-29 cm.

ORIGIN OF DISEOUILIBRIUM (FO-RICH) OLIVINE POPULATION IN **HAWAIITE SAMPLES**

An outstanding question that emerges from the results obtained in this study is what is the origin of the Mg-rich disequilibrium olivines in all Cima hawaiites, including those lavas with entrained peridotite xenoliths. As noted earlier, a Mg-rich disequilibrium olivine population was also found in a similar suite of intraplate hawaiite lavas (the Sangangüey basalts) in western Mexico (Díaz-Bravo et al., 2014; Mesa and Lange, 2021). Mesa and Lange (2021) examined five hypotheses to explain their origin: (1) incorporation of olivine xenocrysts from disaggregated peridotite, (2) unusually high melt oxidation state, (3) the effect of dissolved carbonate on lowering Fe2+-MgK_D(olivine-melt) values (e.g., Dasgupta et al., 2007), (4) disequilibrium olivine composition due to kinetics of rapid growth, and (5) incorporation of olivine xenocrysts due to magma mixing. The same five hypotheses are evaluated below to explain the disequilibrium olivine population in the Cima hawaiites from this study.

The first hypothesis to explain the high-Fo olivines (which fail equilibrium tests: Table 3A) in the Cima hawaiites (Fig. 15) is that they are xenocrysts derived from mantle peridotite xenoliths. This model is inconsistent with the high

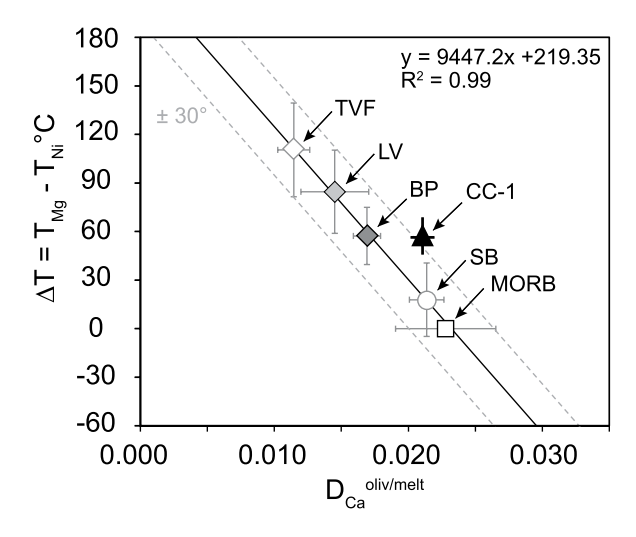


Figure 16. Plot of $\Delta T = (T_{Mg} T_{Ni}$) versus $D_{Ca}^{\text{oliv/liq}}$ for the single high-MgO Dish Hill sample (Cima volcanic field, California, USA) (CC-1) that passes the K_D liquidus tests for equilibrium. Plotted for comparison are the average values for basalts from the Mexican arc (Tancítaro volcanic field, TVF; Pu et al., 2017), Long Valley (LV; Jolles and Lange, 2021), Big Pine (BP; Brehm and Lange, 2020), Sangangüey of western Mexico (SB; Mesa and Lange, 2021), and mid-ocean ridge basalt (MORB) (Allan et al., 1989;

Pu et al., 2017). A strong positive linear correlation ($R^2 = 0.99$) is observed between TVF, LV, BP, SB, and MORB. oliv/liq—olivine/liquid.

CaO contents (>0.20 wt%) of these olivine crystals compared to olivine grains from mantle xenoliths (<0.13 wt%; Wilshire and Trask, 1971; Shervais et al., 1973; Wilshire et al., 1991; Luffi et al., 2009) (Fig. 8). The difference in CaO content as a tool to distinguish between olivine phenocrysts and xenocrysts has long been noted in the literature (e.g., Simkin and Smith, 1970; Norman and Garcia, 1999; Housh et al., 2010). Moreover, the presence of diffusion-limited growth textures (Fig. 11) and complex zoning patterns of P in these high-Fo olivine crystals (Fig. 12) further supports their origin as phenocrysts that grew from a liquid. Therefore, the hypothesis that they are xenocrysts derived from disaggregated mantle peridotite is not viable for the Cima hawaiites.

A second model is that the hawaiite host melts had a higher oxidation state than OFM, leading to lower Fe²⁺ contents in the melt, which would enable the high-Fo olivines to pass the Fe2+-MgK_D(olivine-melt) equilibrium test. However, for this to be the case, a progressive increase in Fe³⁺/Fe^T ratios, from 0.33 to 0.44 with decreasing MgO content in the hawaiites, would be required. Such high oxidations states correspond to Δ QFM values of +2.2 to +3.3, which are inconsistent with the presence of ilmenite in most of the Cima hawaiites. Moreover, the results from the Fe-Ti two-oxide oxybarometer of Ghiorso and Evans (2008) applied to all possible pairs of ilmenite and titanomagnetite that pass the Bacon and Hirschmann (1988) equilibrium test indicate an oxidation state \leq QFM. Finally, Fe³⁺/Fe^T ratios of 0.33–0.44 are inconsistent with reported melt Fe3+/FeT ratios of \sim 0.17 in olivine-hosted melt inclusions from Cima hawaiites (based on V-partitioning; Plank

and Forsyth, 2016). In summary, all available evidence contradicts this hypothesis.

A third possibility is that the high-Fo olivines in the Cima hawaiites reflect the role of dissolved carbonate in the melt, which is known to lower $^{\rm Fe2+-Mg}K_{\rm D}$ (olivine-melt) values (e.g., Dasgupta et al., 2007). Although carbonate may have played a role in the mantle origin of intraplate basanites, the concentrations of dissolved CO2 that are required to affect $^{\rm Fe2+-Mg}K_{\rm D}$ values by ≤ 0.12 units far exceed CO2 solubility limits at crustal depths. Maximum CO2 concentrations analyzed in Cima olivine-hosted melt inclusions (\leq 2412 ppm; Plank and Forsyth, 2016) are too low to affect $^{\rm Fe2+-Mg}K_{\rm D}$ values by more than \sim 0.01 unit. Therefore, this possibility is also not supported by the evidence.

A fourth hypothesis is that Fo contents in olivine are too high relative to hawaiite host bulk compositions due to rapid, disequilibrium growth of olivine. This hypothesis stems from the observation of textural disequilibrium, which provides evidence of diffusion-limited rapid growth of olivine (Figs. 10-13). However, the experiments conducted by Pu et al. (2021), where samples were held superliquidus and then rapidly dropped below the liquidus and held for 8-24 h, grew large, sparse olivine crystals with diffusionlimited growth textures, and all pass olivine-melt equilibrium tests. Moreover, the fact that all 10 basalts from the Big Pine volcanic field studied by Brehm and Lange (2020), including those containing mantle xenoliths and olivine phenocrysts with diffusion-limited growth patterns, all pass the olivine-melt equilibrium test at the liquidus indicates that kinetic disequilibrium cannot be the explanation for the Mg-rich olivine population in the Cima hawaiite samples.

A fifth and final hypothesis is that the high-Fo olivines in the Cima hawaiites were inherited from a more Mg-rich melt (i.e., basanite similar to Dish Hill CC-1; Table 1) and incorporated into the hawaiites during magma mixing. In this scenario, the high-Fo olivines are phenocrysts that grew from a high-MgO (9-10 wt%) melt, similar to those erupted at Dish Hill, Pisgah Crater, and Amboy Crater (Figs. 5 and 6), which then mixed with a low-MgO melt (3-4 wt%, similar to Group 1b, Farmer et al., 1995). If magma mixing is the cause of the high-Mg olivine population in the Cima hawaiites, then their thin Fe-rich rims, along with the rapid magma transport rates inferred from entrained xenoliths, requires that magma mixing between the high- and low-MgO melts must have occurred within days (or less) of eruption (e.g., Hartley et al., 2016).

CONSTRAINTS ON TEMPERATURE-PRESSURE CONDITIONS OF MAGMA MIXING: APPLICATION OF CLINOPYROXENE-LIQUID (CPX-LIQ) THERMOMETRY AND BAROMETRY

Because the Dish Hill samples from this study are devoid of clinopyroxene phenocrysts and the low-MgO endmember liquids were crystal free prior to mixing, it appears that all clinopyroxene growth in the hawaiites must have occurred after mixing. Evidence that the low-MgO endmember was phenocryst free at the time of mixing is the absence (in the mixed Cima hawaiites) of olivine phenocrysts that range from Fo50-65 or plagioclase phenocrysts of andesine-oligoclase composition, both of which are expected phenocrysts in mugearites (e.g., Nelson and Carmichael, 1984; Mesa and Lange, 2021). Here, the hypothesis that the most Mg-rich clinopyroxene population in each hawaiite sample grew immediately after mixing (i.e., grew from a liquid composition closely represented by the whole-rock composition, namely the mixture of a high-MgO liquid with only sparse olivine phenocrysts and a low-MgO liquid) is examined by applying the Fe2+-MgK_D (cpx-liq) and diopside-hedenbergite (Di-Hd) equilibrium tests discussed in Neave and Putirka (2017) and Scruggs and Putirka (2018).

The clinopyroxene-liquid thermometry and barometry results are summarized in Table 4, where the composition of the most Mg-rich clinopyroxene that passes equilibrium tests (when paired with the corresponding whole-rock composition) is reported. Also shown are the calculated temperatures (±45 °C) from Putirka (2008; Equation 33) and pressures (±0.14 GPa) from Neave and Putirka (2017; Equation 1). Among the five Cima samples for which clinopyroxene analyses were obtained, four passed the equilibrium

TABLE 4. COMPOSITION OF THE MOST MG-RICH CLINOPYROXENE PHENOCRYST THAT PASSES EQUILIBRIUM TESTS WITH WR LIQUIDS

Oxide (wt%)	Cima-3	Cima-8	Cima-1	Cima-2	Cima-5
Crystal	cpx 28 (NS)	cpx 16 (NS)	cpx 2 (SZ)	cpx 19 (NS)	none
SiO ₂	47.81	47.32	50.68	48.95	
TiO ₂	1.71	1.62	0.71	1.73	
$Al_2\bar{O}_3$	7.45	7.55	4.76	4.33	
Cr ₂ O ₃	0.71	0.84	0.35	0.13	
FeŌ	5.69	6.28	7.12	7.51	
MnO	0.11	0.12	0.16	0.16	
MgO	14.58	14.76	14.77	14.87	
CãO	21.00	20.50	20.84	21.49	
Na ₂ O	0.66	0.63	0.97	0.42	
Total	99.72	99.61	100.38	99.59	
Mg#	82.0	80.7	78.7	77.9	
The	rmometry (Eq. 33; Put	irka, 2008) Baroı	metry (Eq. 1; Neave	and Putirka, 2017)	
*Fe-MgK _D (cxp-liq)	0.29	0.29	0.31	0.31	
†DiHd error	-0.03	-0.02	-0.02	0.00	
§T (°C) ±45	1113	1112	1145	1147	
P (GPa) ±0.14	0.82	0.81	0.51	0.41	

Notes: WR-whole rock; cpx-liq-clinopyroxene-liquid; Eq.-Equation.

*Fe-MgK_D (cpx-WR liquid) within 0.27 ± 0.04 .

§Note that a variation in ± 45 °C, changes calculated pressures within ± 0.04 GPa.

tests (Cima-3, -8, -1, and -2), which enables application of thermometry and barometry at the onset of clinopyroxene growth immediately after mixing. The temperature results range from $\sim\!1110\!-\!1140\,^{\circ}\mathrm{C}$ (Table 4), which are geologically reasonable since low-MgO mugearite melts have liquidus temperatures of $\sim\!1000\,^{\circ}\mathrm{C}$ (Mesa and Lange, 2021) and high-MgO basanite melts have liquidus tem-

peratures of \sim 1200 °C (this study; $T_{\rm Ni}=1196$ °C for CC-1). The corresponding barometry results range from \sim 0.8 GPa for two samples (Cima-3 and -8) and \sim 0.5–0.4 GPa for two others (Cima-1 and -2), which places the location of mixing at lower to middle crustal depths and requires that the low-MgO endmember melts (mugearite liquids) must have formed at these depths as well.

ORIGIN OF CIMA HAWAIITES: MIXING OF HIGH-MgO BASANITES WITH LOW-MgO MUGEARITES

The hypothesis of magma mixing to explain the high-Fo disequilibrium olivine population in all hawaiites from the Cima volcanic field is consistent with their linear trends in major- and traceelement concentration variation diagrams versus wt% MgO (Figs. 5 and 6). A similar process of magma mixing was demonstrated by Glazner et al. (1991) for two suites of intraplate lavas (~8.5-4.5 wt% MgO) erupted from nearby Pisgah and Amboy craters. Crystal fractionation was precluded in both cases based on Sr and Nd isotopic values that vary co-linearly with MgO content for each volcanic center (Fig. 17). Glazner et al. (1991) established that the high-MgO endmember melts were derived from the asthenosphere, whereas the low-MgO melts must have been formed by partial melting of mafic lower crust to explain the shift in Sr and Nd isotopic values. In that study, the experimental work of Baker and Eggler (1987) is cited as evidence that partial melts of gabbroic lower crust, under relatively dry and reducing conditions, have compositions that overlap the low-MgO mixing endmember at Pisgah and Amboy craters.

A similar model of magma mixing has been established in the literature for the origin of the

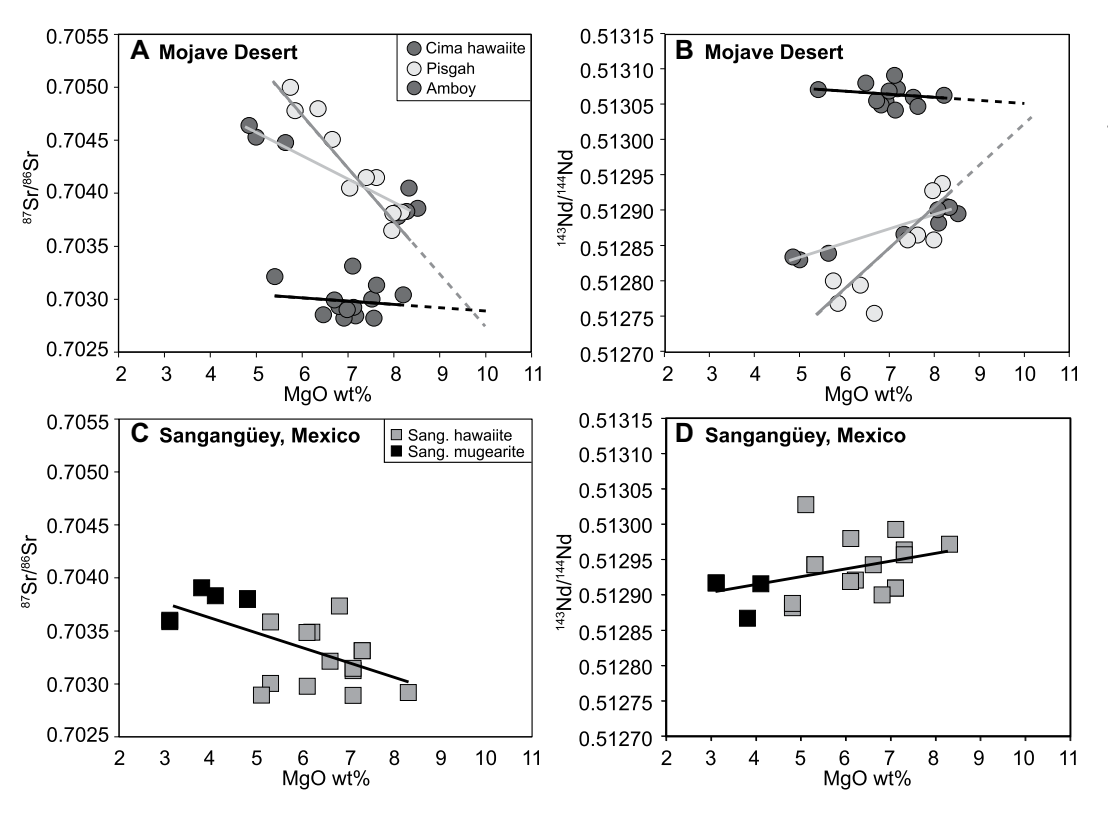


Figure 17. (A) Isotopic ratios of 87Sr/86Sr and 143Nd/144Nd versus whole-rock MgO (wt%) for alkaline basalts from the Mojave Desert including the Cima hawaiites (Farmer et al., 1995) and Pisgah and Ambov craters (Glazner et al., 1991), Cima volcanic field, California, USA. For the Pisgah and Amboy suites, the systematic change in isotopic composition with decreasing MgO content requires that the low-MgO mixing endmember is a partial melt of mafic lower crust (Glazner et al., 1991). Note that the extrapolated high-MgO endmember for the Pisgah and Cima suites have overlapping Sr and Nd isotopic compositions. (B) A similar plot for the Sangangüey alkaline suite reported in the literature (Verma and Nelson, 1989; Gómez-Tuena et al., 2014; and Díaz-Bravo et al., 2014), which requires that the low-MgO mixing endmember is a partial melt of mafic lower crust.

[†]Diopside-hedenbergite (DiHd) error; equilibrium test (≤0.03) from Scruggs and Putirka (2018).

intraplate Sangangüey hawaiites in western Mexico, which also contain a disequilibrium (too Fo-rich) olivine population (Díaz-Bravo et al., 2014; Mesa and Lange, 2021). Similar to what is seen among the Cima volcanic suite (Figs. 5 and 6), Nelson and Carmichael (1984) noted that the Sangangüey lavas display remarkably linear trends among most majorand trace-element variation diagrams with MgO content. Moreover, Verma and Nelson (1989) showed that the Sangangüey suite displayed a progressive shift in Sr and Nd isotopic values with MgO content, which requires involvement of pre-existing mafic crust (Fig. 17). Mesa and Lange (2021) emphasized, as noted in Glazner et al. (1991), that partial melting of mafic lower crust driven by the influx of relatively dry and reduced basaltic melts (in contrast to hydrous and oxidized basalts that form at subduction zones), favors clinopyroxene as a residual phase (in contrast to hornblende and titanomagnetite), which leads to partial melts with relatively low-SiO₂ and elevated FeO contents, a key characteristic of mugearite liquids.

In summary, the evidence available for the Cima hawaiites, both from this study and Farmer et al. (1995), strongly supports the same mixing origin as that deduced for the Pisgah and Amboy lavas (e.g., Glazner et al., 1991) as well as the Sangangüey hawaiites in western Mexico (e.g., Nelson and Carmichael, 1984; Verma and Nelson, 1989; Mesa and Lange, 2021). The results in Figure 17 support a common high-MgO $(\sim 10 \text{ wt\%})$ endmember melt for the Cima and Pisgah suites based on the overlap of their respective Sr and Nd isotopic values extrapolated to \sim 10 wt% MgO. Although the Cima hawaiites do not display a systematic variation in Sr isotopic composition with MgO content (Fig. 17, Group 1a; Farmer et al., 1995), a partial melting origin for the low-MgO endmember (mugearites) is not precluded. The gabbroic xenoliths analyzed by Mukasa and Wilshire (1997), which are entrained in the Cima hawaiites, have isotopic signatures that render them plausible representatives of the mafic lower crust that partially melted to form the low-MgO endmember that mixed with the high-MgO basaltic melts to form the Cima hawaiites.

Note that the Group 1b Cima mugearites (ca. 3–5 Ma; Dohrenwend et al., 1984; Turrin et al., 1985) are too old to be erupted equivalents of the mugearite melts that mixed with high-MgO melts to form the Group 1a Cima hawaiites that erupted between 0 and 1 Ma. They also have Srisotopic values that are too high (Fig. 2).

The main conclusion drawn in this study (i.e., the Cima hawaiites formed by magma mixing) follows that presented in Glazner et al. (1991) for the origin of lavas erupted at Pisgah Crater

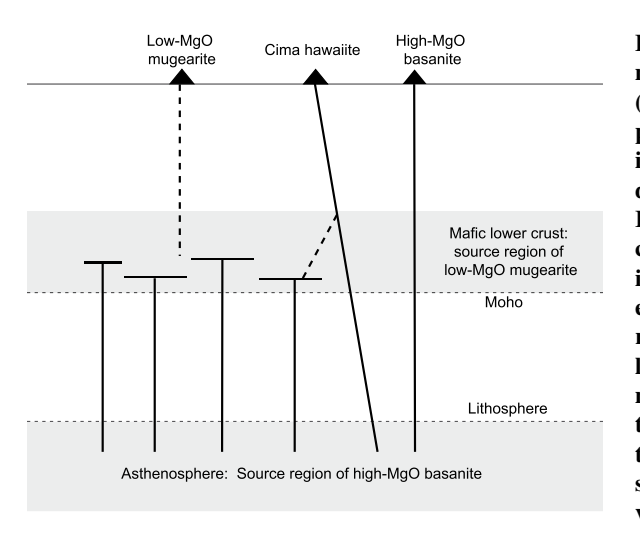


Figure 18. Schematic diagram modified from Mesa and Lange (2021) illustrating the proposed process for rapid magma mixing and phenocryst growth during ascent along fractures. In this proposed model, two compositionally distinct melts including a high-MgO basanite endmember (occasionally carrying mantle xenoliths) and a low-MgO mugearite liquid that mix along intersecting fractures en route to the surface. In this model, Cima-hawaii type samples from this study (Cima volcanic field, California, USA) are hypothesized to be a mix-

ture of a partial melt of the mafic lower crust and a partial melt of the asthenosphere, which mix rapidly during ascent along fractures.

and Amboy Crater, with one key exception. The presence of peridotite xenoliths in several Cima hawaiites requires a different physical model for how the mixing of high- and low-MgO melts occurred. Glazner et al. (1991) proposed a region in the middle crust where high-MgO melts ponded due to neutral buoyancy, which induced partial melting of the lower crust to form low-MgO melts, which then mixed with the high-MgO melts to form the hawaiites erupted at Pisgah and Amboy craters. However, mixing of magmas in a crustal reservoir cannot explain the eruption of large peridotite xenoliths in several of the Cima hawaiite samples, because the intersection of a basaltic dike, with entrained mantle xenoliths, into a broad, partially molten region would have dissipated the dike velocity of the xenolith-bearing melt. An alternative model is that magma mixing occurred during ascent along intersecting fractures.

Evidence for Rapid Magma Mixing During Ascent Along Fractures

As noted above, all the Cima hawaiite samples from this study contain an unusually high-Fo olivine population, which indicates that the high-MgO basalt endmember must have begun to crystallize olivine prior to mixing. The fact that only thin Fe-rich rims are found on the most Mg-rich olivine xenocrysts in most hawaiite samples (Fig. 11) is consistent with magma mixing in fractures, en route to eruption. Because Fe²⁺-Mg diffusion is relatively rapid at temperatures between 1100 and 1200 °C, such thin Ferich rims indicates time scales of days or less between mixing and eruption (e.g., Hartley et al., 2016). The process that is proposed (shown

schematically in Fig. 18) involves two compositionally distinct melts (high-MgO basalt and low-MgO mugearite) initially ascending along separate fracture systems, which subsequently intersect en route to the surface, leading to mixing of the two melts (to form hawaiite) as they continue their ascent along a common fracture to the surface.

Two additional lines of evidence support the model that is schematically illustrated in Figure 18. First, the diffusion-limited growth textures of most olivine phenocrysts (Figs. 12 and 13), as well as clinopyroxene (Fig. S4), are consistent with an undercooling scenario (Brehm and Lange, 2020), which could not develop in a slowly cooling magma chamber. Second, the occurrence of entrained peridotite xenoliths in low-MgO (~5-6 wt%) Cima hawaiites precludes mixing in a stalled magma reservoir. Therefore, magma mixing between a high-MgO endmember melt with entrained peridotite and a low-MgO endmember (i.e., mugearite; partial melt of mafic lower crust under dry, reducing conditions; Glazner et al., 1991) must have occurred during ascent. A similar process of magma mixing within fractures during ascent (Fig. 18) was proposed for the Sangangüey hawaiites in western Mexico (Mesa and Lange, 2021), and it may be a relatively common mechanism in regions of extension.

As an aside, it is worth noting that the expected increase in the bulk viscosity of the mixed hawaiite melt, relative to high-MgO basanite melt, is not expected to affect the successful transport of mantle xenoliths to the surface. An increase in melt viscosity will slow the settling rate of the xenolith out of the host melt (Equation 2) and thus compensate for any slowing of

the ascent velocity of the mixed melt, due to an increase in melt viscosity, during fracture-propagated transport to the surface.

CONCLUSIONS

Several key conclusions can be drawn regarding the origin of the Cima hawaiites and Dish Hill basanites, which are listed below.

- (1) Several lines of evidence indicate that all olivine phenocrysts in the Cima hawaiites and Dish Hill basanites grew rapidly during ascent to the surface along fractures and not over a prolonged period in a stalled crustal reservoir. The strongest support for this conclusion is the presence of dense mantle peridotite xenoliths erupted at the surface in both the low-MgO Cima hawaiites and Dish Hill basanites, which precludes stalling of the magma for any significant period of time during ascent. Additionally, diffusion-limited growth textures are observed in olivine BSE images (e.g., hopper, skeletal), and X-ray intensity maps of P (e.g., dendritic/ oscillatory), as well as BSE images of clinopyroxene (e.g., vermiform, sector-zoning). Diffusion-limited growth textures are consistent with rapid phenocryst growth during ascent, under an effective undercooling ($\Delta T_{eff} = T_{liquidus} - T_{melt}$) (e.g., Brehm and Lange, 2020), which cannot develop in a magma chamber.
- (2) When the $^{\text{Fe2+-Mg}}K_D$ (olivine-melt) and $^{\text{Mg-}}$ MnK_D(olivine-melt) liquidus tests are applied by pairing the most Mg-rich olivine composition in each sample and the whole-rock composition (assuming a melt $Fe^{3+}/Fe^{T} = 0.16$ based on Fe-Ti oxide oxybarometry), the single high-MgO basanite from Dish Hill (CC-1) is the only sample that passes both tests. Notably, all Cima hawaiites in this study fail both liquidus tests, as they contain a population of olivine that is too forsteritic to be in equilibrium with the wholerock composition. While multiple hypotheses were tested to evaluate the origin of this high-Fo olivine population, the only viable hypothesis is that they are olivine xenocrysts inherited from a more Mg-rich melt via mixing.
- (3) Olivine-melt thermometry and hygrometry were applied to the single high-MgO Dish Hill basanite that passes the $^{\rm Fe2+-Mg}K_{\rm D}({\rm olivine-melt})$ liquidus test. The temperature $(T_{\rm Ni})$ and melt $\rm H_2O$ content calculated at the onset of phenocryst growth (i.e., the liquidus) are 1196 °C and 1.4 wt%, respectively. This water content matches that analyzed directly in olivine hosted melt inclusions (Plank and Forsyth, 2016).
- (4) With temperature and melt water content known, the calculated minimum ascent velocity for the Dish Hill basanite is ≥0.3–4.9 km/h, which is required to successfully erupt 5–20 cm diameter mantle xenoliths without them set-

tling out. This result constrains the basanite transit time through the 36 km thick crust to be \leq 7–119 h (<1–5 days).

- (5) There is abundant evidence that supports magma mixing as a plausible explanation for the formation of the low Mg# Cima hawaiites (which entrain mantle xenoliths) presented in this study. A similar hypothesis was presented in the literature to explain the formation of other hawaiites erupted in the Mojave Desert including those at Amboy and Pisgah craters (Glazner et al., 1991). Main lines of evidence that support the hypothesis of magma mixing for the Cima hawaiites are (1) linear trends in major- and trace-element variation plots with MgO (Figs. 5 and 6) and (2) the presence of an olivine population in all Cima hawaiites that is too forsteritic to be in chemical equilibrium with the wholerock composition. A viable hypothesis is that the Cima hawaiites result from magma mixing of a high-MgO basanite melt and a low-MgO mugearite melt. This hypothesis explains the presence of high-Fo disequilibrium olivine (i.e., xenocrysts) in all of the Cima hawaiites.
- (6) Abundant evidence points to the onset of clinopyroxene growth in the hawaiite melts immediately after mixing. Therefore, clinopyroxene-melt barometry applied to the Cima hawaiites constrains the depth at which mixing of the two endmember melts occurred. Results point to depths in the lower and middle crust (0.8–0.4 GPa), which also constrains the origin of the low-MgO endmember melt (mugearite) to these depths as well.
- (7) Isotopic evidence supports a common mechanism of partial melting of mafic lower crust under dry, reducing conditions for the origin of the low-MgO endmember melt (mugearite) among several alkaline volcanic fields, including the Cima, Pisgah, and Amboy suites in the Mojave Desert and the Sangangüey suite in western Mexico (see Figs. 2 and 17).
- (8) Notably, magma mixing to form the Cima hawaiites must have occurred on the order of days or less prior to eruption based on (1) the presence of mantle peridotite xenoliths in many of the low Mg # hawaiites, (2) the absence of significant Fe-rich rims on the most Mg-rich olivine composition (i.e., mixed phenocrysts) in each sample, and (3) diffusion-limited growth textures in olivine and clinopyroxene phenocrysts, which are indicative of rapid growth during ascent along a fracture.

DATA AVAILABILITY STATEMENT

Data sets for the research presented in this study including whole-rock major- and traceelements, as well as microprobe analyses of all phases, are included in this paper and its supplemental information. All data are also archived in the EarthChem data repository (https://doi.org/10.26022/IEDA/112219).

ACKNOWLEDGMENTS

We are grateful to Keith Putirka and Terry Plank for their constructive comments, which led to significant improvements of this manuscript. We thank Dr. Owen Neill for his expertise and assistance in collecting high-quality X-ray intensity maps of olivine on the electron microprobe. This study was supported by the National Science Foundation (grants EAR-2125941 and EAR-1551344).

REFERENCES CITED

- Allan, J.F., Batiza, R., Perfit, M.R., Fornari, D.J., and Sack, R.O., 1989, Petrology of lavas from the Lamont seamount chain and adjacent East Pacific rise, 10° N: Journal of Petrology, v. 30, p. 1245–1298, https://doi.org/10 .1093/petrology/30.5.1245.
- Almeev, R.R., Holtz, F., Koepke, J., Parat, F., and Botcharnikov, R.E., 2007, The effect of H₂O on olivine crystallization in MORB: Experimental calibration at 200 Mpa: The American Mineralogist, v. 92, p. 670– 674, https://doi.org/10.2138/am.2007.2484.
- Armytage, R.M.G., Brandon, A.D., Peslier, A.H., and Lapen, T.J., 2014, Osmium isotope evidence for Early to Middle Proterozoic mantle lithosphere stabilization and concomitant production of juvenile crust in Dish Hill, CA peridotite xenoliths: Geochimica et Cosmochimica Acta, v. 137, p. 113–133, https://doi.org/10.1016/j.gca.2014.04.017.
- Armytage, R.M.G., Brandon, A.D., Andreasen, R., and Lapen, T.J., 2015, Evolution of Mojavian mantle lithosphere influenced by Farallon plate subduction: Evidence from Hf and Nd isotopes in peridotite xenoliths from Dish Hill, CA: Geochimica et Cosmochimica Acta, v. 159, p. 264–284, https://doi.org/10.1016/j.gca .2015.03.038.
- Asimow, P.D., and Ghiorso, M.S., 1998, Algorithmic modifications extending MELTS to calculate subsolidus phase relations: The American Mineralogist, v. 83, p. 1127– 1132, https://doi.org/10.2138/am-1998-9-1022.
- Bacon, C.R., and Hirschmann, M.M., 1988, Mg/Mn partitioning as a test for equilibrium between coexisting Fe-Ti oxides: The American Mineralogist, v. 73, p. 57–61.
- Baker, D.R., and Eggler, D.H., 1987, Compositions of anhydrous and hydrous melts coexisting with plagioclase, augite, and olivine or low-Ca pyroxene from 1 atm to 8 kbar: Application to the Aleutian volcanic center of Atka: The American Mineralogist, v. 72, p. 12–28.
- Banfield, J.F., Dyar, M.D., and McGuire, A.V., 1992, The defect microstructure of oxidized mantle olivine from Dish Hill, California: The American Mineralogist, v. 77, p. 977–986.
- Baziotis, I., Asimow, P.D., Ntaflos, T., Boyce, J.W., McCubbin, F.M., Koroneos, A., Perugini, D., Flude, S., Storey, M., Liu, Y.S., Klemme, S., and Berndt, J., 2017, Phosphorus zoning as a recorder of crystal growth kinetics: Application to second-generation olivine in mantle xenoliths from the Cima Volcanic Field: Contributions to Mineralogy and Petrology, v. 172, no. 58, https://doi.org/10.1007/s00410-017-1376-7.
- Baziotis, I., Xydous, S., Asimow, P.D., Mavrogonatos, C., Flemetakis, S., Klemme, S., and Berndt, J., 2019, The potential of phosphorus in clinopyroxene as a geospeedometer: Examples from mantle xenoliths: Geochimica et Cosmochimica Acta, v. 266, p. 307–331, https://doi .org/10.1016/j.gca.2019.04.024.
- Blondes, M.S., Reiners, P.W., Ducea, M.N., Singer, B.S., and Chesley, J., 2008, Temporal-compositional trends over short and long time-scales in basalts of the Big Pine Volcanic Field, California: Earth and Planetary Science Letters, v. 269, p. 140–154, https://doi.org/10.1016/j .epsl.2008.02.012.
- Blundy, J., Melekhova, E., Ziberna, L., Humpreys, M.C.S., Cerantola, V., Brooker, R.A., McCammon, C.A., Pichavant, M., and Ulmer, P., 2020, Effect on the Fe-Mg-Mn

- exchange between olivine and melt and an oxybarometer for basalts: Contributions to Mineralogy and Petrology, v. 175, no. 103, https://doi.org/10.1007/s00410-020-01736-7.
- Brehm, S.K., and Lange, R.A., 2020, Evidence of rapid phenocryst growth of olivine during ascent in basalts from the Big Pine Volcanic Field: Application of olivine-melt thermometry and hygrometry at the liquidus: Geochemistry, Geophysics, Geosystems, v. 21, no. 10, https://doi.org/10.1029/2020GC009264.
- Dasgupta, R., Hirschmann, M.M., and Smith, N.D., 2007, Partial melting experiments of peridotite + CO₂ at 3 Gpa and genesis of alkalic ocean island basalts: Journal of Petrology, v. 48, p. 2093–2124, https://doi.org/10 .1093/petrology/egm053.
- Davis, G.A., Fowler, T.K., Bishop, K.M., Brudos, T.C., Friedman, S.J., Burbank, D.W., Parke, M.A., and Burchfiel, B.C., 1993, Pluton pinning of an active Miocene detachment fault system, eastern Mojave Desert, California: Geology, v. 21, p. 627–630, https://doi.org /10.1130/0091-7613(1993)021<0627:PPOAAM>2 .3.CO;2.
- Díaz-Bravo, B.A., Gómez-Tuena, A., Ortega-Obregón, C., and Pérez-Arvizu, O., 2014, The origin of intraplate magmatism in the western Trans-Mexican volcanic belt: Geosphere, v. 10, p. 340–373, https://doi.org/10 .1130/GES00976.1.
- Dohrenwend, J.C., McFadden, L.D., Turrin, B.D., and Wells, S.G., 1984, K-Ar dating of the Cima volcanic field, eastern Mojave Desert, California: Late Cenozoic volcanic history and landscape evolution: Geology, v. 12, p. 163–167, https://doi.org/10.1130 /0091-7613(1984)12<163:KDOTCV>2.0.CO;2.
- Farmer, G.L., Glazner, A.F., Wilshire, H.G., Wooden, J.L., Pickthorn, W.J., and Katz, M., 1995, Origin of late Cenozoic basalts at the Cima volcanic field, Mojave Desert, California: Journal of Geophysical Research. Solid Earth, v. 100, p. 8399–8415, https://doi.org/10 .1029/95JB00070.
- Fitton, J.G., James, D., Kempton, P.D., Ormerod, D.S., and Leeman, W.P., 1988, The role of lithospheric mantle in the generation of late Cenozoic basic magmas in the western united states: Journal of Petrology, special volume, no. 1, p. 331–349, https://doi.org/10.1093/petrology/Special_Volume.1.331.
- Fitton, J.G., James, D., and Leeman, W.P., 1991, Basic magmatism associated with Late Cenozoic extension in the western United States: Compositional variations in space and time: Journal of Geophysical Research. Solid Earth, v. 96, p. 13,693–13,711, https://doi.org/10.1029 /91JB00372.
- Gavrilenko, M., Herzberg, C., Vidito, C., Carr, M.J., Tenner, T., and Ozerov, A., 2016, A calcium-in-olivine geohygrometer and its application to subduction zone magmatism: Journal of Petrology, v. 57, p. 1811–1832, https://doi.org/10.1093/petrology/egw062.
- Gazel, E., Plank, T., Forsyth, D.W., Bendersky, C., Lee, C.T.A., and Hauri, E.H., 2012, Lithosphere versus asthenosphere mantle sources at the Big Pine Volcanic Field, California: Geochemistry, Geophysics, Geosystems, v. 13, no. 6, https://doi.org/10.1029 /2012GC004060.
- Gee, L.L., and Sack, R.O., 1988, Experimental petrology of melilite nephelinites: Journal of Petrology, v. 29, p. 1233–1255, https://doi.org/10.1093/petrology/29 .6.1233.
- Ghiorso, M.S., and Evans, B.W., 2008, Thermodynamics of rhombohedral oxide solid solutions and a revision of the Fe-Ti two-oxide geothermometer and oxygen-barometer: American Journal of Science, v. 308, p. 957– 1039, https://doi.org/10.2475/09.2008.01.
- Ghiorso, M.S., and Sack, R.O., 1995, Chemical mass transfer in magmatic processes IV. A revised and internally consistent thermodynamic model for the interpolation and extrapolation of liquid-solid equilibria in magmatic systems at elevated temperatures and pressures: Contributions to Mineralogy and Petrology, v. 119, p. 197–212, https://doi.org/10.1007/BF00307281.
- Glazner, A.F., Farmer, G.L., Hughes, W.T., Wooden, J.L., and Pickthorn, W., 1991, Contamination of basaltic magma by mafic crust at Amboy and Pisgah Craters, Mojave Desert, California: Journal of Geophysical Research.

- Solid Earth, v. 96, p. 13,673–13,691, https://doi.org/10 .1029/91JB00175.
- Gómez-Tuena, A., Díaz-Bravo, B., Vázquez-Duarte, A.V., Pérez-Arvizu, O., and Mori, L., 2014, Andesite petrogenesis by slab-derived plume pollution of a continental rift, in Gómez-Tuena, A., Straub, S.M., and Zellmer, G.F., Orogenic Andesites and Crustal Growth: Geological Society of London Special Publications, v. 385, p. 65–101, https://doi.org/10.1144/SP385.4.
- Hartley, M.E., Morgan, D.J., MacLennan, J., Edmonds, M., and Thordarson, T., 2016, Tracking timescales of short-term precursors to large basaltic fissure eruptions through Fe-Mg diffusion in olivine: Earth and Planetary Science Letters, v. 439, p. 58–70, https://doi.org /10.1016/j.epsl.2016.01.018.
- Heinrich, W., and Besch, T., 1992, Thermal history of the upper mantle beneath a young back-arc extensional zone: Ultramafic xenoliths from San Luis Potosí, Central Mexico: Contributions to Mineralogy and Petrology, v. 111, p. 126–142, https://doi.org/10.1007 /BF00296583.
- Hofmann, A.W., and Jochum, K.P., 1996, Source characteristics derived from very incompatible trace elements in Mauna Loa and Mauna Kea basalts, Hawaii Scientific Drilling Project: Journal of Geophysical Research. Solid Earth, v. 101, p. 11,831–11,839, https://doi.org/ /10.1029/95JB03701.
- Housh, T.B., Aranda-Gómez, J.J., and Luhr, J.F., 2010, Isla Isabel (Nayarit, México): Quaternary alkalic basalts with mantle xenoliths erupted in the mouth of the Gulf of California: Journal of Volcanology and Geothermal Research, v. 197, p. 85–107, https://doi.org/10.1016/j .jvolgeores.2009.06.011.
- Hui, H., and Zhang, Y., 2007, Toward a general viscosity equation for natural anhydrous and hydrous silicate melts: Geochimica et Cosmochimica Acta, v. 71, p. 403–416, https://doi.org/10.1016/j.gca.2006.09.003.
- Ishibashi, H., and Sato, H., 2010, Bingham fluid behavior of plagioclase-bearing basaltic magma: Reanalyses of laboratory viscosity measurements of Fuji 1707 basalt: Journal of Mineralogical and Petrological Sciences, v. 105, p. 334–339, https://doi.org/10.2465/jmps .100611.
- Johnson, E.R., Wallace, P.J., Delgado Granados, H., Manea, V.C., Kent, A.J.R., Bindeman, I.N., and Donegan, C.S., 2009, Subduction-related volatile recycling and magma generation beneath Central Mexico: Insights from melt inclusions, oxygen isotopes and geodynamic models: Journal of Petrology, v. 50, p. 1729–1764, https://doi .org/10.1093/petrology/egp051.
- Jolles, J.S.R., and Lange, R.A., 2021, Temperatures and water contents of Long Valley, CA basalts: Application of olivine-melt thermometry and hygrometry at the liquidus: Journal of Volcanology and Geothermal Research, v. 417, https://doi.org/10.1016/j.jvolgeores 2021.107298.
- Kelley, K.A., and Cottrell, E., 2012, The influence of magmatic differentiation on the oxidation state of Fe in a basaltic arc magma: Earth and Planetary Science Letters, v. 329–330, p. 109–121, https://doi.org/10.1016/j .epsl.2012.02.010.
- Kleest, C., and Webb, S.L., 2021, Influence of CO₂ on the rheology of melts from the Colli Albani Volcanic District (Italy): Foidite to phonolite: Contributions to Mineralogy and Petrology, v. 176, no. 92, https://doi.org/10 .1007/s00410-021-01838-w.
- Kouchi, A., Sugawara, Y., Kashima, K., and Sunagawa, I., 1983, Laboratory growth of sector zones clinopyroxenes in the system CaMgSi₂O₆-CaTiAl₂O₆: Contributions to Mineralogy and Petrology, v. 83, p. 177–184, https://doi.org/10.1007/BF00373091.
- Kress, V.C., and Carmichael, I.S.E., 1991, The compressibility of silicate liquids containing Fe₂O₃ and the effect of composition, temperature, oxygen fugacity and pressure on their redox states: Contibutions to Mineralogy and Petrology, v. 108, p. 82–92, https://doi.org/10.1007/BF00307328.
- Lange, R.A., 1996, Temperature independent thermal expansivities of sodium aluminosilicate melts between 713 and 1835 K: Geochimica et Cosmochimica Acta, v. 60, p. 4989–4996, https://doi.org/10.1016/S0016-7037(96)00301-8.

- Lange, R.A., and Carmichael, I.S.E., 1990, Hydrous basaltic andesites associated with minette and related lavas in Western Mexico: Journal of Petrology, v. 31, p. 1225– 1259, https://doi.org/10.1093/petrology/31.6.1225.
- Lofgren, G., 1974, An experimental study of plagioclase crystal morphology: Isothermal crystallization: American Journal of Science, v. 274, p. 243–273, https://doi .org/10.2475/ajs.274.3.243.
- Luffi, P., Saleeby, J.B., Lee, C.-T.A., and Ducea, M.N., 2009, Lithospheric mantle duplex beneath the central Mojave Desert revealed by xenoliths from Dish Hill, California: Journal of Geophysical Research. Sold Earth, v. 114, no. B3, https://doi.org/10.1029/2008JB005906.
- Luhr, J.F., and Aranda-Gómez, J.J., 1997, Mexican peridotite xenoliths and tectonic terranes: Correlations among vent location, texture, temperature, pressure, and oxygen fugacity: Journal of Petrology, v. 38, p. 1075–1112, https://doi.org/10.1093/petroj/38.8.1075.
- Médard, E., and Grove, T.L., 2008, The effect of H₂O on the olivine liquidus of basaltic melts: Experiments and thermodynamic models: Contributions to Mineralogy and Petrology, v. 155, p. 417–432, https://doi.org/10 .1007/s00410-007-0250-4.
- Mesa, J., and Lange, R.A., 2021, Origin of alkali olivine basalts and hawaiites in the west Mexican arc: Evidence of rapid phenocryst growth and magma mixing during ascent along fractures: Geosphere, v. 17, p. 1563–1588, https://doi.org/10.1130/GES02365.1.
- Milman-Barris, M.S., Beckett, J.R., Baker, M.B., Hofmann, A.E., Morgan, Z., Crowley, M.R., and Stolper, E., 2008, Zoning of phosphorus in igneous olivine: Contributions to Mineralogy and Petrology, v. 155, p. 739–765, https://doi.org/10.1007/s00410-007-0268-7.
- Mukasa, S.B., and Wilshire, G., 1997, Isotopic and trace element compositions of upper mantle and lower crustal xenoliths, Cima volcanic field, California: Implications for evolution of the subcontinental lithospheric mantle: Journal of Geophysical Research. Solid Earth, v. 102, p. 20,133–20,148, https://doi.org/ 1/10.1029/97JB01518.
- Neave, D.A., and Putirka, K.D., 2017, A new clinopyroxeneliquid barometer, and implications for magma storage pressures under Icelandic rift zones: The American Mineralogist, v. 102, p. 777–794, https://doi.org/10 .2138/am-2017-5968.
- Nelson, S.A., and Carmichael, I.S.E., 1984, Pleistocene to recent alkalic volcanism in the region of Sangangüey volcano, Nayarit, Mexico: Contributions to Mineralogy and Petrology, v. 85, p. 321–335, https://doi.org/10 .1007/BF01150290.
- Norman, M.D., and Garcia, M.O., 1999, Primitive magmas and source characteristics of the Hawaiian plume: Petrology and geochemistry of shield picrites: Earth and Planetary Science Letters, v. 168, p. 27–44, https://doi .org/10.1016/S0012-821X(99)00043-6.
- Ochs, F.A., and Lange, R.A., 1999, The density of hydrous magmatic liquids: Science, v. 283, p. 1314–1317, https://doi.org/10.1126/science.283.5406.1314.
- Peterman, Z.E., Carmichael, I.S.E., and Smith, A.L., 1970, Strontium isotopes in Quaternary basalts of southeastern California: Earth and Planetary Science Letters, v. 7, p. 381–384, https://doi.org/10.1016/0012-821X(70)90078-6.
- Petford, N., Kerr, R.C., and Lister, J.R., 1993, Dike transport of granitoid magmas: Geology, v. 21, p. 845–848, https://doi.org/10.1130/0091-7613(1993)021<0845:DTO GM>2.3.CO;2.
- Phillips, F. M., 2003, Cosmogenic 36Cl ages of Quaternary basalt flows in the Mojave Desert, California, USA: Geomorphology, v. 53, p. 199–208, https://doi.org/10 __1016/S0169-555X(02)00328-8.
- Plank, T., and Forsyth, D.W., 2016, Thermal structure and melting conditions in the mantle beneath the Basin and Range province from seismology and petrology: Geochemistry, Geophysics, Geosystems, v. 17, p. 1312– 1338, https://doi.org/10.1002/2015GC006205.
- Pu, X., Lange, R.A., and Moore, G., 2017, A comparison of olivine-melt thermometers based on DMg and Dni: The effects of melt composition, temperature, and pressure with applications to MORBs and hydrous arc basalts: The American Mineralogist, v. 102, p. 750–765, https:// doi.org/10.2138/am-2017-5879.

- Pu, X., Moore, G.M., Lange, R.A., and Touran, J.P., 2021, Experimental evaluation of a new H₂O-independent thermometer based on olivine-melt Ni partitioning at a crustal pressure: The American Mineralogist, v. 106, p. 235–250, https://doi.org/10.2138/am-2020-7014.
- Putirka, K., 2008, Excess temperatures at ocean islands: Implications for mantle layering and convection: Geology, v. 36, no. 4, p. 283–286, https://doi.org/10.1130/G24615A.1.
- Putirka, K.D., 2016, Rates and styles of planetary cooling on Earth, Moon, Mars, and Vesta, using new models for oxygen fugacity, ferric-ferrous ratios, olivine-liquid Fe-Mg exchange, and mantle potential temperature: The American Mineralogist, v. 101, p. 819–840, https://doi.org/10.2138/am-2016-5402.
- Putirka, K.D., Perfit, M., Ryerson, F.J., and Jackson, M.G., 2007, Ambient and excess mantle temperatures, olivine thermometry, and active vs. passive upwelling: Chemical Geology, v. 241, p. 177–206, https://doi.org/10.1016 /j.chemgeo.2007.01.014.
- Putirka, K., Jean, M., Cousens, B., Sharma, R., Torrez, G., and Carlson, C., 2012, Cenozoic volcanism in the Sierra Nevada and Walker Lane, California, and a new model for lithosphere degradation: Geosphere, v. 8, p. 265–291, https://doi.org/10.1130/GES00728.1.
- Righter, K., and Carmichael, I.S.E., 1993, Mega-xenocrysts in alkali olivine basalts: Fragments of disrupted mantle assemblages: The American Mineralogist, v. 78, p. 1230–1245.
- Roeder, P.L., Poustovetov, A., and Oskarsson, N., 2001, Growth forms and composition of chromian spinel in MORB magma: Diffusion-controlled crystallization of chromian spinel: Canadian Mineralogist, v. 39, p. 397– 416, https://doi.org/10.2113/gscammin.39.2.397.
- Scruggs, M.A., and Putirka, K.D., 2018, Eruption triggering by partial crystallization of mafic enclaves at Chaos Crags, Lassen Volcanic Center, California: The American Mineralogist, v. 103, p. 1575–1590, https://doi.org/10.2138/am-2018-6058.
- Shea, T., Hammer, J.E., Hellebrand, E., Mourey, A.J., Costa, F., First, E.C., Lynn, K.J., and Melnik, O., 2019, Phosphorous and aluminum zoning in olivine: Contrasting behavior of two nominally incompatible trace elements: Contributions to Mineralogy and Petrology, v. 174, no. 85, https://doi.org/10.1007/s00410-019-1618-y.
- Shervais, J.W., Wilshire, H.G., and Schwarzman, E.C., 1973, Garnet clinopyroxenite xenolith from Dish Hill, California: Earth and Planetary Science Letters, v. 19, p. 120–130, https://doi.org/10.1016/0012-821X(73)90106-4.
- Simkin, T.O.M., and Smith, J.V., 1970, Minor-element distribution in olivine: The Journal of Geology, v. 78, p. 304–325, https://doi.org/10.1086/627519.

- Skulski, T., Minarik, W., and Watson, E.B., 1994, Highpressure experimental trace-element partitioning between clinopyroxene and basaltic melts: Chemical Geology, v. 117, p. 127–147, https://doi.org/10.1016 //0009-2541(94)90125-2.
- Smith, A.L., and Carmichael, I.S.E., 1969, Quaternary trachybasalts from southeastern California: The American Mineralogist, v. 54, p. 909–923.
- Sparks, R.S.J., Pinkerton, H., MacDonald, R., 1977, The transport of xenoliths in magmas: Earth and Planetary Science Letters, v. 35, p. 234–238, https://doi.org/10 .1016/0012-821X(77)90126-1.
- Spera, F.J., 1980, Aspects of magma transport, in Hargraves, R.B., ed., Physics of Magmatic Processes: Princeton, New Jersey, Princeton University Press, v. 105, p. 265– 324, https://doi.org/10.1515/9781400854493.265.
- Spera, F.J., 1984, Carbon dioxide in petrogenesis III: Role of volatiles in the ascent of alkaline magma with special reference to xenolith-bearing mafic lavas: Contributions to Mineralogy and Petrology, v. 88, p. 217–232, https:// doi.org/10.1007/BF00380167.
- Toplis, M.J., 2005, The thermodynamics of iron and magnesium partitioning between olivine and liquid: Criteria for assessing and predicting equilibrium in natural and experimental systems: Contributions to Mineralogy and Petrology, v. 149, p. 22–39, https://doi.org/10 .1007/s00410-004-0629-4.
- Turrin, B.D., Dohrenwend, J.C., Wells, S.G., and McFadden, L.D., 1985, Geochronology and eruptive history of the Cima volcanic field, eastern Mojave Desert, California, in Dohrenwend, J.C., ed., Surficial Geology of the Eastern Mojave Desert, California: Reno, Nevada, Geological Society of America 1984 Annual Meeting field trip guidebook, p. 88–100.
- Verma, S.P., and Nelson, S.A., 1989, Isotopic and trace element constraints on the origin and evolution of alkaline and calc-alkaline magmas in the Northwestern Mexican volcanic belt: Journal of Geophysical Research. Solid Earth, v. 94, p. 4531–4544, https://doi.org/10.1029/JB094iB04p04531.
- Welsch, B., Faure, F., Famin, V., Baronnet, A., and Bachèlery, P., 2012, Dendritic crystallization: A single process for all the textures of olivine in basalts?: Journal of Petrology, v. 54, p. 539–574, https://doi.org/10.1093/petrology/egs077.
- Welsch, B., Hammer, J., and Hellebrand, E., 2014, Phosphorus zoning reveals dendritic architecture of olivine: Geology, v. 42, p. 867–870, https://doi.org/10.1130/G35691.1.
- Welsch, B., Hammer, J., Baronnet, A., Jacob, S., Hellebrand, E., and Sinton, J., 2016, Clinopyroxene in postshield Haleakala ankaramite: 2. Texture, compositional zoning and supersaturation in the magma: Contributions to

- Mineralogy and Petrology, v. 171, no. 6, https://doi.org/10.1007/s00410-015-1213-9.
- Wilshire, H.G., and McGuire, A.V., 1996, Magmatic infiltration and melting in the lower crust and upper mantle beneath the Cima volcanic field, California: Contributions to Mineralogy and Petrology, v. 123, p. 358–374, https://doi.org/10.1007/s004100050162.
- Wilshire, H.G., and Trask, N.J., 1971, Structural and textural relationships of amphibole and phlogopite in peridotite inclusions: American Mineralogist, v. 56, p. 240–255.
- Wilshire, H.G., Nielson Pike, J.E., Meyer, C.E., and Schwarzman, E.C., 1980, Amphibole-rich veins in lherzolite xenoliths, Dish Hill and Deadman Lake, California: American Journal of Science, v. 280-A, p. 576–593.
- Wilshire, H., Meyer, C.E., Nakata, J.K., Calk, L.C., Shervais, J.W., Nielson, J.E., and Schwarzman, E.C.,, 1988, Mafic and ultramafic xenoliths from volcanic rocks of the western United States: U.S. Geological Survey Professional Paper 1443, 179 p., https://doi.org/10.3133/pp1443.
- Wilshire, H.G., McGuire, A.V., Noller, J.S., and Turrin, B.D., 1991, Petrology of lower crustal and upper mantle xenoliths from the Cima volcanic field, California: Journal of Petrology, v. 32, p. 169–200, https://doi.org/10 .1093/petrology/32.1.169.
- Wilshire, H.G., Bedford, D.R., and Coleman, T., 2002a, Geologic Map of the Indian Spring Quadrangle, San Bernardino County, California: U.S. Geological Survey Open-File Report 92-181, scale 1:24,000.
- Wilshire, H.G., Bedford, D.R., and Coleman, T., 2002b, Digital version of "Open-file report 92-182: Geologic map of the Marl Mountains Quadrangle, San Bernardino County, California": U.S. Geological Survey Open-File Report 2002-271, scale 1:24,000, https://pubs.er.usgs.gov/publication/ofr02271.
- Wilson, M.R., Kyser, T.K., and Fagan, R., 1996, Sulfur isotope systematics and platinum group element behavior in REE-enriched metasomatic fluids: A study of mantle xenoliths from Dish Hill, California, USA: Geochimica et Cosmochimica Acta, v. 60, p. 1933–1942, https://doi.org/10.1016/0016-7037/96)00069-5.
- Wise, W.S., 1969, Origin of basaltic magmas in the Mojave Desert area, California: Contributions to Mineralogy and Petrology, v. 23, p. 53–64, https://doi.org/10.1007 /BF00371332.

SCIENCE EDITOR: BRAD S. SINGER

Manuscript Received 16 November 2021 Revised Manuscript Received 11 February 2022 Manuscript Accepted 30 March 2022

Printed in the USA